Icarus 353 (2021) 113406

Contents lists available at ScienceDirect

Icarus

journal homepage: www.elsevier.com/locate/icarus

# The current weather and climate of Mars: 12 years of atmospheric monitoring by the Planetary Fourier Spectrometer on Mars Express

Marco Giuranna[a,*], Paulina Wolkenberg[a,b], Davide Grassi[a], Alessandro Aronica[a], Shohei Aoki[a,c,d,e], Diego Scaccabarozzi[f], Bortolino Saggin[f], V. Formisano[a,1]

[a] Istituto di Astrofisica e Planetologia Spaziali (IAPS) – Istituto Nazionale di Astrofisica (INAF), Via del Fosso del Cavaliere 100, Rome 00133, Italy
[b] Centrum Badan Kosmicznych Polska Akademia Nauk, ul. Bartycka 18a, 00 – 716 Warsaw, Poland
[c] Royal Belgian Institute for Space Aeronomy, Avenue Circulaire 3, 1180 Brussels, Belgium
[d] Fonds National de la Recherche Scientifique, rue d'Egmont 5, B-1000 Brussels, Belgium
[e] Department of Geophysics, Graduate School of Science, Tohoku University, Aramaki Aza Aoba 6-3, Sendai, Miyagi 980-8578, Japan
[f] Department of Mechanics, Politecnico di Milano, Campus of Lecco, Lecco, Italy

A B S T R A C T

We used thermal-infrared spectra returned by the Mars Express Planetary Fourier Spectrometer (PFS/MEx) to retrieve atmospheric temperature profiles, surface temperatures, and column-integrated optical depths of dust and water ice. More than 2,500,000 spectra were processed to build this new atmospheric dataset, covering the full range of season, latitude, longitude, and local time. The data presented here span more than six Martian Years (from MY 26, Ls = 331°, 10 January 2004 to MY 33, Ls = 78°, 6 December 2015). We present an overview of the seasonal and latitudinal dependence of the above atmospheric quantities for the relevant period, as well as an assessment of the interannual variability in the current Martian climate. The general effect of suspended dust on atmospheric temperatures observed during the global dust storm of MY 28 is also presented. Atmospheric temperatures and aerosol opacity were successfully retrieved over cold surface areas and in the polar regions, including the polar nights. Rather than the aphelion cloud belt, the most prominent feature one can observe in the climatology of the Martian water ice clouds is the seasonal extent, pattern and thickness of the North polar hoods (NPH), where most of the thickest clouds are observed. The NPH also shows peculiar features, observed in detail here for the first time, with characteristic spatial and seasonal patterns that repeat very similarly every Martian year. By exploiting PFS/MEx capability to perform observations at different local times (LT), this dataset allowed the characterization of how dust and ice cloud optical depths vary throughout the day on Mars. We present observations of the dust daily cycle during non-dusty seasons; the daily variation of water ice opacity in the aphelion cloud belt; and the diurnal variation of the North and South polar hoods. With unprecedented spatial and temporal coverage and details revealed, this dataset offers new challenges to the Martian global circulation models and, at the same time, a new reference for the MYs complementary to those observed by previous orbiters.

## 1. Introduction

The state of a planetary atmosphere can be described by the interdependence of the temperature, pressure and density as a function of the altitude. The knowledge of the vertical temperature profiles is essential for an understanding of the dynamical, thermodynamical, and chemical processes occurring in the atmosphere. In addition, suspended aerosols such as dust and water ice, which are very variable in the Martian atmosphere, strongly affect the radiative transfer, with significant impact on the atmospheric density and temperature, and influence on the large-scale dynamics (e.g., Medvedev et al., 2011; Clancy et al., 2017; Barnes et al., 2017). Thermal infrared observations of the 15-μm $CO_2$ band are commonly used to retrieve atmospheric temperatures at different levels within the atmosphere by exploiting the variation in known optical depth as a function of wavelength across the band. Several instruments have successfully used this approach to retrieve atmospheric temperature profiles, including the InfraRed Interferometer Spectrometer (IRIS) on Mariner 9 (Conrath et al., 1973), the Thermal Emission Spectrometer (TES) on Mars Global Surveyor (MGS) (Conrath et al., 2000; Smith, 2004), the Mars Climate Sounder (MCS) on Mars Reconnaissance Orbiter (MRO) (Kleinböhl et al., 2009), and the Planetary Fourier Spectrometer (PFS) on Mars Express (MEx) (Grassi et al., 2005; Wolkenberg et al., 2018). Wide-band infrared observations covering the 15-μm $CO_2$ band can also be used to infer temperature representative of atmospheric layers around 0.5 mbar pressure level. Examples are the InfraRed Thermal Mapper (IRTM) on Viking Orbiter (Martin and Kieffer, 1979; Wilson and Richardson, 2000) and the THermal EMission Imaging System (THEMIS) on Mars Odyssey (Smith et al., 2003). The amount of aerosols suspended in the atmosphere is preferably described by the vertical density profiles of

* Corresponding author at: IAPS – INAF, Via del Fosso del Cavaliere 100, Rome 00133, Italy.
*E-mail address:* marco.giuranna@iaps.inaf.it (M. Giuranna).
[1] Deceased on 28 March 2016.

https://doi.org/10.1016/j.icarus.2019.113406
Received 7 January 2019; Received in revised form 9 July 2019; Accepted 5 August 2019
Available online 06 August 2019
0019-1035/ 

the suspended particles. Inversion techniques have been developed and applied to limb-geometry observations by the SPectroscopy for the Investigation of the Characteristics of the Atmosphere of Mars (SPICAM) (Rannou et al., 2006), TES (Clancy et al., 2010; Guzewich et al., 2013), the Compact Reconnaissance Imaging Spectrometer for Mars (CRISM) (Smith et al., 2013), and MCS (Kleinböhl et al., 2009, 2011), as well as stellar occultations by SPICAM (Montmessin et al., 2006), to derive information on the vertical distribution of dust and water ice aerosols on Mars. When vertical profiles could not be retrieved, the column-integrated optical depth at given wavelength is provided. This quantity describes the atmospheric opacity in specific wavelengths due to the presence of the suspended aerosols. When the radiance observations are obtained by nadir-viewing instruments, the column-integrated optical depth is the typical product of dust or water ice retrievals, such as those for TES (Smith et al., 2000; Pearl et al., 2001), THEMIS (Smith et al., 2003), and CRISM (Wolff et al., 2009; Douté et al., 2013) observations, as well as those for PFS (Grassi et al., 2005; Zasova et al., 2005; Wolkenberg et al., 2018), SPICAM (Perrier et al., 2006; Mateshvili et al., 2009; Willame et al., 2017) and OMEGA (Määttänen et al., 2009; Madeleine et al., 2012; Douté et al., 2014) nadir observations from the Mars Express orbiter.

Currently, several datasets of atmospheric parameters, collected in a variety of different ways, are available for Mars. Data returned by orbiting spacecrafts can usually be collected systematically on a global scale and provide the most complete datasets. Atmospheric temperatures and aerosol opacities have been consistently retrieved for several Martian years from remote-sensing infrared observations by TES (from Ls ~ 100° of MY 24 to Ls ~ 80° of MY 27; Smith, 2004, 2008), THEMIS (still collecting data since Ls ~ 330° of MY 25; Smith, 2009), and MCS (still collecting data since Ls = 111.3° of MY 28; McCleese et al., 2010). These datasets, combined with ever more accurate global circulation models, have allowed us to improve our understanding of the main physical processes that control the current Martian climate, circulation, and dynamics. However, these datasets are highly heterogeneous, as they have been created using data from different instruments having different geometric views, spatial and temporal coverage, as well as different observing wavelengths (e.g., Montabone et al., 2015), making the quantitative comparison of the retrieved quantities by the different instruments in the different Martian years more difficult. Each dataset has also different limitations, being either temporal, spatial, or vertical limitations. TES retrievals cover only two full Martian years (Smith, 2004, 2008). THEMIS retrievals of atmospheric temperatures rely on a single band which is representative of a wide range of heights centred at about 0.5 mbar (Smith, 2009). MCS limb retrievals have the advantage of allowing the retrieval of vertical profiles of temperature and aerosols up to ~80 km, but have the disadvantage of not being able to observe the first kilometres above the ground, the lowest altitude depending on the angle of observation and the amount of suspended aerosols (Kleinböhl et al., 2009). As a consequence, e.g., the MCS dust profiles cannot be retrieved down to the surface, and the dust in the un-retrieved part of the profile can account for a significant fraction of the total dust column (Montabone et al., 2015). In addition, a common limitation of the above datasets is that they have a very discrete coverage in local time, due to the choice of orbit geometry. MGS and MRO have Sun-synchronous polar orbits, which allow observations at two fixed local times (except when crossing the poles), namely 2:00 AM and 2:00 PM for MGS, and 3:00 AM and 3:00 PM for MRO. The local time of the THEMIS observations is also quite limited, being typically between 4:00 and 6:00 PM (Smith, 2009).

In this paper, we present the new dataset of atmospheric temperature profiles, surface temperatures, and column-integrated dust and water ice retrievals by PFS. More than 2,500,000 spectra have been processed to build this new dataset, covering the full range of season, latitude, longitude, and local time for more than six full Martian years. PFS performed observations at all local times, allowing detailed investigation of the daily variation of suspended dust and ice. Atmospheric temperatures and aerosols opacity are also successfully retrieved over cold surface areas and in the polar regions, including the polar nights, where most of the previous datasets suffered limited retrieval capability.

## 2. PFS dataset and retrievals

The Planetary Fourier Spectrometer (PFS) (Formisano et al., 2005) on Mars Express (MEx) (Wilson and Chicarro, 2004) has been observing the Martian atmosphere since January of 2004, Ls = 331.18° of MY 26. It has now provided nearly continuous monitoring of conditions in the Martian atmosphere for over seven full Martian years and it is still performing measurements at the time of writing. PFS is a double-pendulum infrared Fourier spectrometer optimized for atmospheric studies. It has two distinct spectral channels operating simultaneously and covering the wavenumber range between 200 and 2000 $cm^{-1}$ (Long Wavelength Channel, hereafter LWC) and 2000–8300 $cm^{-1}$ (Short Wavelength Channel, hereafter SWC). Both channels have a sampling step of 1 $cm^{-1}$ and a spectral resolution of ~1.3 $cm^{-1}$, when no apodization function is applied, and ~1.8 $cm^{-1}$ when Hamming function is applied to the measured interferograms (as in the case of the present work). The MEx spacecraft is orbiting Mars in a polar orbit having an inclination of 87°, a pericentre altitude of ~240 km and an orbital period of ~7.5 h. The instantaneous field of view (IFOV) is about 1.52° (Full Width Half Maximum, FWHM) for the SWC and 2.69° (FWHM) for the LWC, which corresponds to a spatial resolution of, respectively, 6.5 and 11.5 km at the pericentre. Additional details about the PFS design, specifications, and operation may be found in Formisano et al. (2005). The spectral and radiometric calibration procedure for both channels has been discussed in detail by Giuranna et al. (2005a, 2005b). The current PFS calibration pipeline makes use of the instrumental phase-based method for Fourier transform spectrometer measurements processing recently developed by Saggin et al. (2011).

Thermal-infrared spectra returned by PFS LWC are well suited for retrieval of the thermal structure of the atmosphere from the surface to about 60 km, as well as of the column-integrated optical depth of suspended dust and water ice. The infrared spectrum of Mars can be ideally divided into two parts: the shorter wavelengths dominated by the reflected solar radiation, and the longer wavelengths dominated by the thermal radiation emitted by the atmosphere and the surface of the planet. In the case of Mars, the boundary of these two regions is near 3 μm. The SWC and LWC channels of the PFS instrument practically correspond to these two parts of the Martian infrared spectrum (Giuranna et al., 2005a, 2005b). The PFS LWC is particularly useful to retrieve key atmospheric parameters. Indeed, information on vertical temperature profiles in Martian atmosphere can be retrieved from measurements of the thermal radiation emitted by the planet in the spectral range corresponding to the main absorption band of the gaseous $CO_2$ (the main constituent of the Martian atmosphere, with ~95% of abundance), which is centred around 667 $cm^{-1}$ (15 μm). The wide absorption bands of dust and water ice centred around 1075 $cm^{-1}$ (9.3 μm) and 825 $cm^{-1}$ (12 μm), respectively, can be effectively used to derive integrated optical depths. Moreover, the atmosphere of Mars is particularly transparent around two spectral regions, centred at ~300 $cm^{-1}$ and ~1300 $cm^{-1}$, which are then particularly convenient for the retrieval of surface temperatures.

The atmospheric parameters presented in this work were retrieved by means of the algorithm for the scientific analysis of individual calibrated PFS LWC measurements originally developed by Grassi et al. (2005). Here we used an improved version of the original algorithm, described in Wolkenberg et al. (2018). The improved algorithm makes use of the optimal estimation method coupled with the Bayesian approach (Levenberg, 1944; Marquardt, 1963; Rodgers, 2000), and has been optimized for the retrieval of dust and ice opacity during strong dust storms and in the aphelion cloud belt (Wolkenberg et al., 2018). Our retrieval scheme exploits the entire range 275–1300 $cm^{-1}$ to

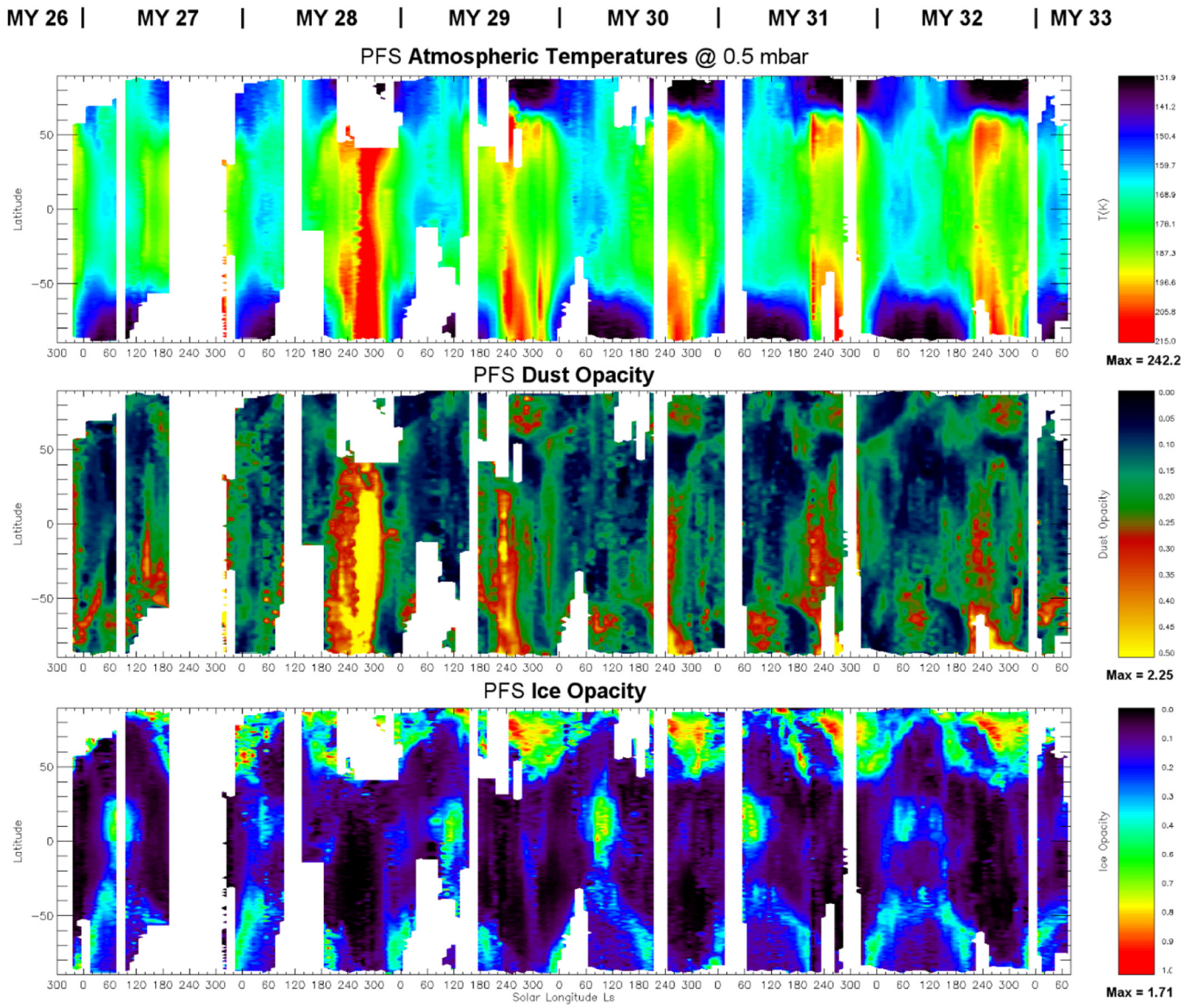


**Fig. 1.** Zonal-mean atmospheric temperatures at 0.5 mbar (top), integrated dust opacity at 1075 $cm^{-1}$ (9.3 μm) (middle), and integrated ice opacity at 825 $cm^{-1}$ (12 μm) (bottom), as a function of latitude and season for different Martian years. The dust opacity is normalized to a reference pressure level of 6.1 mbar.

perform simultaneous, self-consistent retrieval of the following atmospheric parameters (state vector elements): (a) surface temperature; (b) air temperature profile; (c) integrated dust content; (d) integrated water ice content.

The computation of synthetic spectra to be compared (best-fit) to the PFS observations relies on the DISORT solver implemented in the ARS code, which was specifically developed for the analysis of PFS spectra (Ignatiev et al., 2005). DISORT (Discrete Ordinates Radiative Transfer Program for a Multi-Layered Plane-Parallel Medium) is a general and versatile plane-parallel radiative transfer program applicable to problems from the ultraviolet to the radar regions of the electromagnetic spectrum (Stamnes et al., 1988), which include a full treatment of atmospheric multiple scattering by suspended particles. Standard Mie theory (e.g., Bohren and Huffman, 1983) is used to calculate single-scattering quantities (e.g., single scattering albedo, extinction cross-section, etc.) of suspended ice and dust to be used as input parameters for ARS. For water ice, we use optical constants from Hansen et al. (1997) and Hansen (2005) and size distribution from Wolff and Clancy (2003). For dust, we use optical constants from Hansen (2003, 2005) and size distribution from Clancy et al. (2003). We use HITRAN 2012 (Rothman et al., 2013) as spectroscopic database for the calculation of the gaseous absorption coefficients. The synthetic spectra are obtained by performing the line by line computation and then filtering the result with the PFS instrumental line shape (ILS; Giuranna et al., 2005a). Hamming apodization is applied to the PFS interferograms. It is common practice in Fourier transform spectroscopy to multiply the measured interferogram by an apodizing function in order to reduce the amount of ringing present in the resulting ILS (Davis et al., 2001). This reduces the spectral resolution a bit (from ~1.3 $cm^{-1}$ when no apodization function is applied, to about 1.8 $cm^{-1}$ when Hamming function is applied to the interferograms, in the case of PFS), but also reduces the instrumental noise and the magnitude of the side-lobes in the instrumental line shape, which are a direct result of the finite maximum optical difference in the measured interferograms (Naylor and Tahic, 2007). The PFS ILS, both for the apodized and unapodized cases, was measured in laboratory by pointing PFS to a monochromatic source (a mercury lamp) for different temperatures. The final result is a function of slightly asymmetric sin-cardinal type (Giuranna et al., 2005a).

The typical quality of PFS spectra modelling for different thermal

conditions of the atmosphere is presented in Giuranna et al. (2008). Uncertainty in the retrieved atmospheric temperatures is typically ~1 K in the ~10–30 km altitude range, and larger (1–4 K) at lower and higher altitudes. The relatively high spectral resolution of PFS allows the detection of several different thermal gradients in the atmosphere, as shown by the effective modelling in the same spectrum of absorbing and emitting Q-branches inside the 15-μm $CO_2$ absorption band (Fig. 1 in Giuranna et al., 2008). Noteworthy, the relatively high sensitivity of PFS allows the retrieval of the above-mentioned atmospheric parameters also over cold surfaces and in the night side, including the polar regions and the polar nights. Examples of PFS spectra of the polar night atmospheres in selected regions and are provided in the Appendix. PFS spectra acquired over the ACB and during the MY 28 GDS are also shown in the Appendix. Examples of PFS spectra modelling by the improved retrieval algorithm during global dust storms and for different loads of atmospheric dust can be found in Wolkenberg et al. (2018). These authors also investigated the retrieval uncertainty for aerosols opacity and found it is mainly related to the values of the surface temperature. Namely, larger uncertainty is observed for low surface temperatures (or, equivalently, for low signal-to-noise ratio spectra), as one would expect. An in-depth analysis revealed that the PFS dataset can actually be divided in two sub-datasets, based on the surface temperatures. The temperature threshold is found to be 220 K for dust and 210 K for ice. In the "warm regime", the typical single-retrieval uncertainty ranges from ~0.02–0.06 for dust, and is around 0.01 for water ice (Wolkenberg et al., 2018). In the "cold regime", the typical single-retrieval uncertainty is ~0.11 for dust, and 0.06 or lower for water ice (Wolkenberg et al., 2018).

## 3. Results

In this section we present the dataset of atmospheric parameters retrieved by PFS for > 6 full MYs. We used PFS data collected from Ls = 331° of MY 26 (January 10th 2004) to Ls = 78° of MY 33 (December 6th 2015) to derive surface temperatures, vertical temperature profiles, and integrated dust and ice content in the Martian atmosphere. The zonally-averaged values of atmospheric temperatures at 0.5 mbar (~25 km), as well as of dust and ice opacity as a function of season (Ls) and latitude are shown in Fig. 1. The data were binned in 5° Ls × 1° latitude bins. The dust opacity is normalized to a reference pressure level to eliminate the effect of topographic inhomogeneities. Each retrieved opacity value is divided by the surface pressure at the appropriate location, local time, and season, and then multiplied by 6.1 mbar (often considered as the mean Martian surface pressure), the value used for the reference pressure level. For the surface pressure we used PRES0, a routine provided with the Mars Climate Database (MCD v5.2; Millour et al., 2015; Forget et al., 1999), which makes use of high resolution (32 pix/deg.) MOLA topography to estimate the surface pressure with high accuracy. White areas in Fig. 1 indicate observational gaps (lack of data) caused by different reasons during the various years of MEx operations, including spacecraft safe modes, spacecraft mass memory issues, solar conjunctions, eclipse seasons, and other MEx- and PFS-related temporary issues.

Repeatable patterns are observed every year for each of the retrieved quantities. The northern spring and summer (Ls = 0–180°, also referred to as the aphelion season since aphelion (Ls = 71°) occurs near the northern summer solstice (Ls = 90°)) are cool, relatively dust free, and with extensive water ice clouds occurring every year (Fig. 1). On the contrary, the southern spring and summer (Ls = 180–360°) are warm and dusty, relatively ice free (except for the polar hoods), and with regular occurrence of regional dust storms. The reduced insolation during the aphelion season, which is a consequence of the increased distance of Mars to the Sun due to the eccentricity of its orbit, is a primary driver of the overall cooler seasonal climate. Wolkenberg et al. (2011) compared atmospheric average temperature profiles retrieved by PFS to those retrieved by TES during the overlapping period and spatial coverage (the two instruments operated simultaneously from Ls = 331° of MY 26 to Ls = 84° of MY 27) and found an overall good agreement. In particular, at the 50 Pa pressure level, temperature differences were mostly within the 1-σ deviation and always within ± 5 K between 40° S and 40° N latitude.

One of the most striking features we can observe in Fig. 1 is the large increase of the atmospheric temperatures (top panel) during the southern spring and summer of MY 28, when a global dust storm occurred. In this period, the zonally-averaged atmospheric temperatures at 0.5 mbar (~25 km), an altitude at which the temperature response to dust aerosols is particularly evident (Smith, 2004), are up to 30 K warmer than in the other years observed by PFS (top panel of Fig. 1). Moreover, during the global dust storm of MY 28, the maximum of dust activity occurred between 270° and 305° of solar longitude, much later than in the other Martian years (middle panel of Fig. 1). In this period, high amounts of dust persist over most of the tropical and sub-tropical regions, and the maximum zonally-averaged dust opacity exceeds 2.

Regional dust storms occur regularly every Martian year. The strongest regional-scale dust event is observed in MY 29, when large (> 0.7) zonally-averaged dust opacity is observed, especially at sub-tropical latitudes and during the seasonal range Ls = 220–260° (middle panel of Fig. 1). Wolkenberg et al. (2018) compared dayside, zonal-mean dust opacities obtained from TES and PFS and found good consistency between opacities obtained from the two instruments, most of the retrievals being distributed within the combined standard deviation. The same authors made use of the same dataset of atmospheric parameters as presented in this work to characterize the dust activity on Mars from MY 27 to MY 32, as well as its effects on the atmospheric temperatures and circulation.

The bottom panel of Fig. 1 shows the seasonal and latitudinal dependence of water ice cloud optical depth as observed by PFS for different Martian years. The most prominent seasonal features that are observed every year are the polar hoods in middle to high latitudes of both hemispheres, and the aphelion cloud belt (ACB) at low latitudes. Mars' polar hoods were observed in the past mainly by ground-based telescopes, providing limited information about the spatial and seasonal extent as well as of the involved processes in their formation (James et al., 1990; Martin et al., 1992; Akabane et al., 1993). Observations of the south polar hood (SPH), in particular, were spoiled by Mars being tilted away from Earth during the fall and winter seasons (Martin et al., 1992; James et al., 1990). Early spacecraft observations from Mariner 9 and Viking orbiters were also quite limited (James et al., 1992). TES and MOC instruments on the Mars Global Surveyor made observations of both the north polar hood (NPH) and the SPH. However, both datasets were restricted to ± 60° N latitude during fall and winter seasons due to either the difficulty in obtaining ice retrievals over a cold surface (Smith, 2004), or the absence of sunlight within the terminator circles and the difficulty of distinguishing clouds from the bright icy surfaces (Wang and Ingersoll, 2002; Benson et al., 2006). PFS retrievals of water ice cloud optical depth presented in bottom panel of Fig. 1 cover the full seasonal and latitudinal range for more than six consecutive Martian years and allow us to establish the detailed spatial and seasonal extent and patterns of the polar hoods, as well as to investigate the processes involved in their formation. The NPH shows peculiar features, described in detail in the next section, with characteristic spatial and seasonal patterns that repeat very similarly every Martian year.

The ACB is a water ice cloud band that encircles Mars longitudinally at latitudes ranging from about 10° S to 30° N during the northern spring and summer (Ls = 0–180°; aphelion season). The ACB forms when water vapour sublimated from the north polar cap reaches the tropics and is incorporated into the upwelling branch of the solsticial Hadley cell, becoming saturated at relatively low condensation levels compared to those at the perihelion season when atmospheric temperatures are warmer (Clancy et al., 1996; Richardson et al., 2002; Montmessin et al., 2004). The ACB is an important component of the current Martian climate system, playing a key role in the seasonal

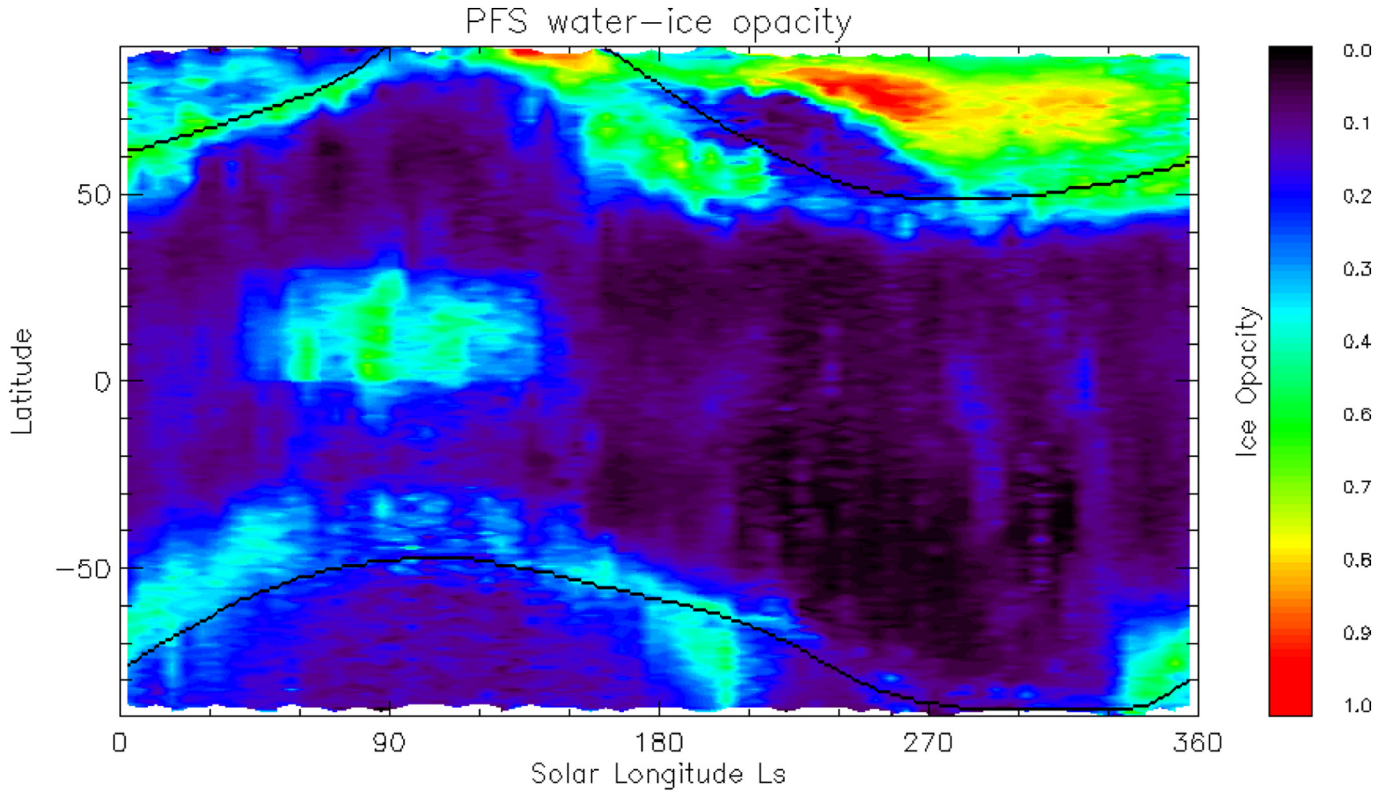


**Fig. 2.** Seasonal and latitudinal variation of zonal-mean water ice opacity observed by PFS. Data collected from all observed Martian years (Fig. 1) were binned in 5° Ls × 1° latitude bins. The black curve shows the climatological latitude of the seasonal $CO_2$ polar cap edges (Titus, 2005; Titus and Cushing, 2014).

evolution of the water vapour cycle (Richardson et al., 2002) by controlling its cross-equatorial transport (Montmessin et al., 2004), and in the atmospheric and surface thermal structure through its radiative effects (Wilson et al., 2007, 2008; Madeleine et al., 2012). The aphelion cloud belt is observed by PFS every year. The large dependence of the ice opacity with the local time (see below) is the main reason for the seemingly large inter-annual variation of the ACB (bottom panel of Fig. 1). The south polar hood is often connected by a narrow filament to the ACB during its period of maximum optical depth. Two different seasonal "links" between the south polar hood and the ACB are observed in MY 32 (bottom panel of Fig. 1).

### 3.1. Climatology of water ice clouds

The seasonal and latitudinal variation of water ice cloud optical depth as observed by PFS is shown in Fig. 2. Data collected from all observed Martian years were binned in 5° Ls × 1° latitude bins. From a climatological point of view, the Martian atmosphere outside the polar regions is characterized by relatively-low column-integrated ice opacity from late summer (Ls = ~150°) to the end of the year. In contrast to what has been reported by previous analyses of different datasets, the most prominent feature one can observe is the seasonal extent, pattern and thickness of the North polar hoods, rather than the ACB. Moreover, the polar hoods are observed all year round by PFS in both polar regions, although they show very different characteristics.

The NPH exhibits larger opacities and always extends to the pole, while the SPH is an optically thinner annular ring that basically follows the climatological latitudes of the seasonal (water) ice cap edge. This is in good agreement with both observations by MCS and atmospheric simulations (Benson et al., 2010, 2011; Montmessin et al., 2004; Navarro et al., 2014) and is due to the fact that the southern winter hemisphere is much dryer than its northern counterpart, combined with a less efficient supply of water vapour to the southern polar region (Montmessin et al., 2004; Navarro et al., 2014). Typical zonally-averaged NPH optical depth values throughout the year range from 0.1 to 0.7, with peak opacities larger than 0.8 consistently observed each Martian year in specific areas and seasons. In particular, the largest climatological opacities (up to 1.0) are observed over a latitudinal stripe between ~65–85° N during most of the fall and winter seasons (210–330° Ls). Large cloud opacity is also observed around the north pole in correspondence with the beginning of the northern seasonal frost deposits, especially between 130 and 160° of solar longitude. Zonally-averaged optical depth values of the SPH vary typically from 0.1 to 0.4. Peak opacities up to 0.6–0.7 are consistently observed at two specific seasonal ranges: 180–205° Ls and 330–360° Ls, during which the SPH also extends to the south pole (Fig. 2). This is in remarkably good agreement with recent MCS observations in limb sounding geometry (see Fig. 1e and q in Benson et al., 2010).

The extent of the polar hoods varies with the season. Their boundaries always exceed those of the seasonal $CO_2$ polar caps in either hemispheres (Fig. 2), and rather follow those of the seasonal annuli of water ice observed in both hemispheres by several instruments (Wagstaff et al., 2008; Kuzmin et al., 2012; Bapst et al., 2015). In Fig. 3 we show the spatial distribution of water ice clouds throughout the whole Martian year, in bins of 30° of solar longitude. Data collected from all observed Martian years were binned in 5° longitude × 3° latitude bins. In both hemispheres, the maximum extension is observed around the respective winter solstices, when the SPH boundary reaches ~25° S and the NPH extends down to ~35° N latitude (Fig. 2). However, in proximity of the solstices, the polar hoods also show lower opacity. In particular, low SPH opacities are observed in the seasonal range 50–140° Ls, which corresponds to the period of maximum activity of the aphelion cloud belt (Figs. 2 and 3c–e). In this period, little water vapour is available in the southern polar region, as the southward transport of water forms the low-latitude cloud belt instead of being transported to the southern hemisphere (Clancy et al., 1996; Richardson et al., 2002). The opacity at the edges of the NPH (exceeding the edges of the seasonal $CO_2$ polar caps) also reduces

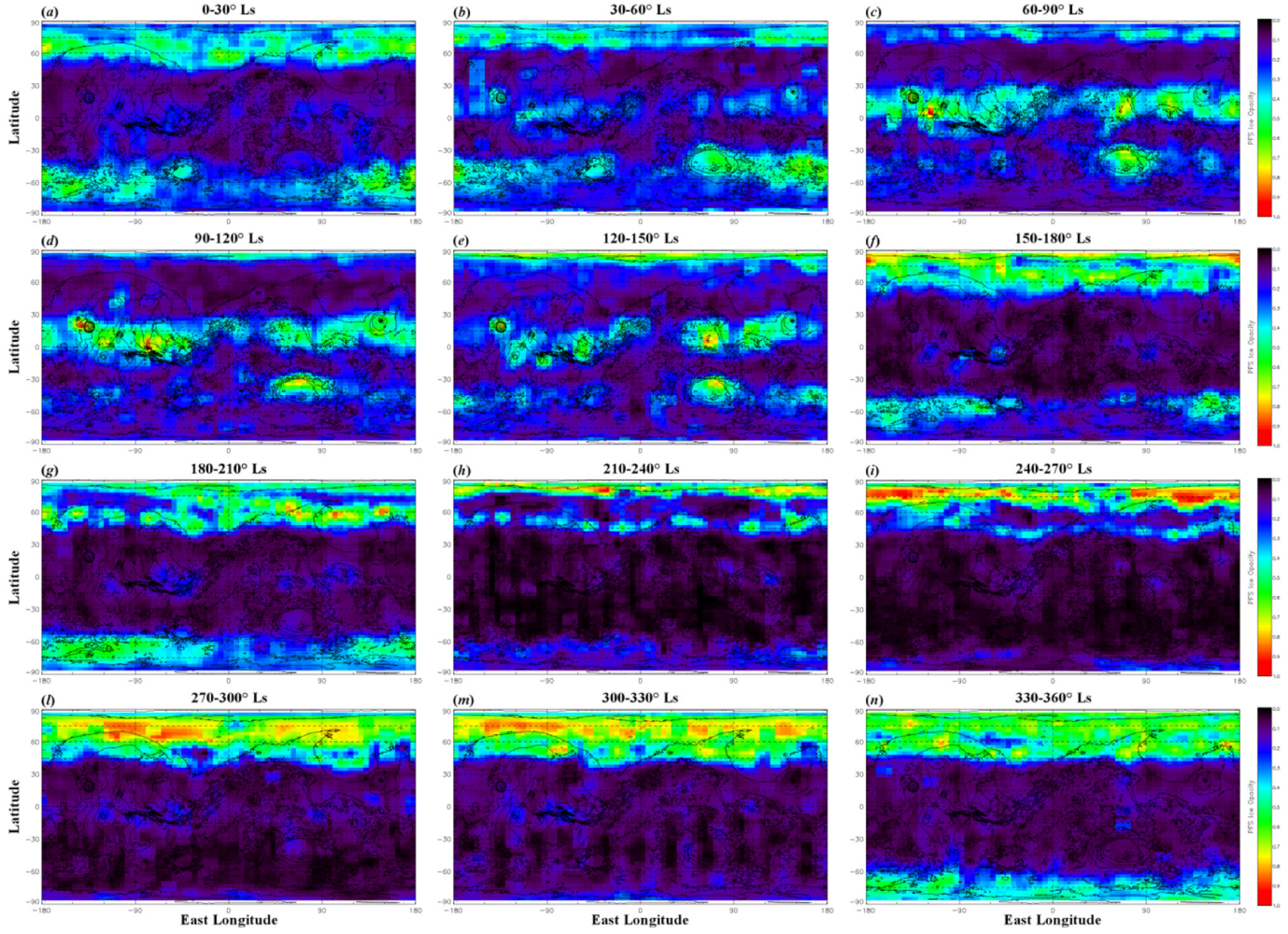


**Fig. 3.** Spatial maps of water ice optical depth measured by PFS at different seasons. The calculations were made using bin sizes of 3° latitude, 5° longitude, and 30° Ls. Data collected from all observed Martian years (Fig. 1) were used. MOLA topographical contours between −8 km and 20 km altitude (for altitude steps of 2 km) with respect to mars aeroid are superimposed (black contours). The colour scale is the same as in Fig. 2. Repeatable patterns are observed every Martian year. Note the region where no ice clouds form in the NPH during the northern fall (panels *f* to *i*). Note also the strong decrease of SPH opacity in correspondence of the period of maximum activity of the aphelion cloud belt (panels *c* to *e*). See text for more details. (For interpretation of the references to colour in this figure legend, the reader is referred to the web version of this article.)

substantially around the winter solstice, from 220° to 280° of solar longitude (Fig. 2), likely due to a significant reduction in wave activity (Montmessin et al., 2004). Thick ice clouds are always observed over Hellas basin during most of the northern spring and summer season (from 30° to 150° of solar longitude) and especially along the northern rim of the crater (Fig. 3b–e), while ice clouds form over Argyre basin during most of the northern spring (Fig. 3a–c). The ACB is observed by the PFS in every Martian year. It reaches peaks in optical depth and extension around Ls = 100°, and gradually dissipates after Ls = 140° (Fig. 3a–g). The latitudinal extend of the ACB (approximately from 10° S to 30° N) coincides with the boundaries of the overturning circulation and its decay is due to an increase of atmospheric temperature at low latitudes and to the transition towards a weaker equinox circulation.

The NPH shows peculiar features, with characteristic spatial and seasonal patterns that repeat very similarly every Martian year. Large opacities (> 0.5) are always observed at latitudes > 80° N, from the summer solstice (Ls = 90°) until the vernal equinox (Ls = 360°) (Figs. 2 and 3d–n). From 270° to 360° Ls, the whole polar region is covered with optically-thick water ice clouds (Fig. 3l–n). However, one can also observe a region where practically no ice clouds form during the entire northern fall (Fig. 2). This “cloud-free” region is observed every Martian year between 170° and 280° Ls (Figs. 1 and 2). It is always ~60-degrees of solar longitude wide but moves latitudinally towards lower latitudes as the season advances (Fig. 2). It is first observed around 170° Ls and 75° N (Fig. 3f). Then, it gradually extends to lower latitudes with the season (Fig. 3g–h), down to ~50° N in the seasonal interval 220–280° Ls (Figs. 2 and 3h–i). A similar feature was identified in the zonally-averaged ice opacity retrieved by TES over the northern polar region (Horne and Smith, 2009).

At the moment, we do not have any straightforward explanation for the NPH features observed by PFS. The agreement between water ice opacities observed by PFS and predicted by Martian GCMs is generally good. In particular, the absolute opacities and seasonal variations of the ACB and the SPH observed by PFS are well reproduced by the models (e.g., Montmessin et al., 2004). However, the absolute opacities and, most importantly, the characteristic spatial and seasonal patterns of the NPH observed by PFS cannot be reproduced by current models, including recent implementations with improved microphysics and radiatively active ice clouds (Navarro et al., 2014; Neary and Daerden, 2017). Benson et al. (2010, 2011) used MCS observations in limb sounding geometry to investigate the Mars' polar hoods and found that the cloud optical depth is more strongly controlled by atmospheric temperature variations rather than by intrinsic fluctuations in water vapour abundance. These authors suggested that NPH clouds were primarily controlled by the temperature structure and formed at the water condensation level. Interestingly enough, MCS observed a sudden

decrease of cloud optical depth and a much poleward confinement of the NPH soon after Ls = 210°, which then persisted for several tens of degrees of solar longitude. This is in remarkably good agreement with PFS observations (Figs. 2 and 3) and was interpreted as due to increased atmospheric temperatures caused by dust storm activity regularly occurring in this period. MCS also observed ice-free regions associated to the descending branch of the Hadley circulation, which were interpreted as due to both the adiabatic warming in the descending branch as well as the desiccation of the atmosphere in the ascending and poleward branches of the circulation (Benson et al., 2011). These interpretations might contribute to the explanation for the presence of the cloud-free region observed by PFS, and for the lower opacity observed at the edge of the NPH in proximity of the winter solstice. However, among the various spatial maps provided by MCS in different seasonal ranges, only those in the seasonal interval 210–225° Ls (Fig. 3d in Benson et al., 2011) overlap temporally with the PFS observations of the cloud-free areas. Unfortunately, those maps have gaps (no data retrieved) in the 60–75° N latitudinal range, which is exactly where the cloud-free region is observed by PFS at that time of the year (Fig. 3h), precluding any direct comparison. The partial inability of water vapour to penetrate into the north polar vortex might also play a role, by preventing the clouds to be formed at higher latitudes (Richardson et al., 2002). However, during the fall and winter seasons, PFS always observes large opacities at latitudes > 80° N, either suggesting that the clouds previously formed around the pole persist for a long time, or that some amount water vapour/ice penetrates the vortex and is transported to higher latitudes (> 80° N), or both. McCleese et al. (2017) made use of an improved algorithm for the retrieval of temperatures and aerosol opacities from MCS limb observations (Kleinböhl et al., 2017) to study the Mars polar atmosphere. These authors reported a significant abundance of water ice in the core of the northern polar vortex, at latitudes > 80° N, and, based on the analysis of individual ice profiles from MCS, concluded that water could enter the vortex from above, possibly transported by the Hadley circulation (McCleese et al., 2017).

### 3.2. Surface temperatures

The sole purpose of this small section is to compare the retrieved surface temperatures with those predicted by the MCD v5.2 and with the climatological latitudes of the seasonal $CO_2$ polar cap edges. In Fig. 4 we show the seasonal evolution of the zonal-mean surface temperatures measured by PFS. Data collected from all observed Martian years and local times were binned in 5° Ls × 1° latitude bins. The areas where the retrieved surface temperatures range between 140 and 150 K (the expected range of $CO_2$ condensation temperature on Mars) match well with the areas where the surface is covered by the seasonal $CO_2$ ice (Fig. 4a). Each binned value in Fig. 4a is an average of several thousands of PFS values collected in different Martian years and for different local times and atmospheric conditions. We used the Mars Climate Database (MCD v5.2; Millour et al., 2015; Forget et al., 1999) developed at Laboratoire de Météorologie Dynamique (LMD) to extract the surface temperatures at the exact location and time of the single PFS observations. We then binned the simulated temperature in the same way as the PFS data. The difference between the predicted and the measured surface temperatures is shown in Fig. 4b. The agreement is good, the absolute differences being mostly < 5 K. The largest discrepancies are observed at the edges of the receding polar caps after the respective equinoxes, where the model likely fails to predict the actual extent of the seasonal deposits, being either $CO_2$ ice or water ice.

### 3.3. Climatology of dust

In Fig. 5 we show the latitudinal and seasonal evolution of suspended dust on Mars (Fig. 5a) and the zonally-averaged atmospheric temperatures at 0.5 mbar (~25 km; Fig. 5b). PFS data collected from all observed Martian years, except MY 28 when a global dust storm occurred (Fig. 1), were binned in 5° Ls × 1° latitude bins. Although the temperatures respond to the eccentricity of the orbit and distance to the sun, the two quantities in Fig. 5 are linked due to the dust heating the atmosphere. In the following, we will focus on the climatological aspects of Martian dust. An in-depth characterization of the dust activity on Mars from MY 27 to MY 32 as well as of its effects on the atmospheric temperatures and circulation, obtained from the analysis of the same dataset of atmospheric parameters as presented in this work (Fig. 1), can be found in Wolkenberg et al. (2018).

Contrary to what is observed for the ice clouds, the northern spring and summer (Ls = 0–180°) are relatively dust free. Although substantial aerosol opacity is observed in the core of the polar vortex in both polar regions, especially around the winter solstices, it is mostly due to the presence of $CO_2$ ice clouds or hazes rather than dust. The retrieval algorithm used to process PFS data does not yet distinguish between dust in the atmosphere and $CO_2$ ice aerosol. Such a distinction is particularly difficult to achieve because both species have overlapping features in the spectral range here analysed (7.5–25 μm). As a consequence, our data products identify $CO_2$ ice clouds as dust. Similar issues apply to MCS unfiltered dust retrievals (Kleinböhl et al., 2009) and MCS observations of aerosol in the winter high latitudes of both hemispheres were also interpreted as due to $CO_2$ clouds retrieved as dust (McCleese et al., 2010, 2017; Heavens et al., 2011a, 2011b, 2011c).

A region of extremely dust-clear atmosphere separates the dust in the winter tropics from the aerosols in the winter high latitudes. This feature repeats every Martian year and is mainly observed at mid-latitudes (45–60° N) around the northern winter solstice (Ls = 220–310°) (Fig. 5a; see also Wolkenberg et al., 2018). It is not reproduced by any of the current GCMs available for Mars and a complete explanation is still missing. The region of extremely dust clear air corresponds well with the area of the atmosphere heated primarily by the descending branch of the Hadley circulation and was also observed by TES and MCS. Similarly to PFS, TES observed dust-clear annular bands occurring from 45° N to 60° N in the seasonal range 220–310° Ls, and a barely visible counterpart in the South around northern summer solstice (Ls = 90°) (Horne and Smith, 2009). Contrary to PFS and TES, MCS retrievals of density-scaled dust opacity show a broader area of clear atmosphere in the southern hemisphere at Ls = 90° than in the northern one at Ls = 270° (McCleese et al., 2010; Heavens et al., 2011b, 2011c).

PFS regularly observes dynamic dust activity near the edges of the seasonal caps throughout the year in both hemispheres, induced by thermal gradients resulting from the expansion and regression of the polar caps (Fig. 5a). Increased dust storm activity along and inside the cap edges was also observed by MOC and HST visual cameras (Cantor et al., 2001, 2002; Wang et al., 2003; James et al., 1999, 2005), as well as by OMEGA (Douté et al., 2014) and TES (Horne and Smith, 2009), whereas little or no dust is present in the MCS observations at polar cap edge latitudes (Montabone et al., 2015). Flows capable of lifting dust from the surface can be achieved by a variety of conditions at a variety of spatial scales, from cap edge thermal contrasts, to topographic variations, thermal tides, and sublimation of the polar deposits (Siili et al., 1999; Toigo et al., 2002; Spiga and Lewis, 2010; Mulholland et al., 2015). In particular, large temperature variations generate large pressure gradients, initiating the movement of air from one location to another. The larger the horizontal pressure gradient force, the stronger the wind, which can efficiently lift the surface dust up to the atmosphere. At the cap edges, the lateral temperature heterogeneities due to cold icy deposits and warm defrosted surface can cause high surface friction and vertical mixing thus injecting dust in the atmosphere (Spiga and Lewis, 2010; Siili et al., 1999). Cap-edge winds, analogues to terrestrial sea breeze circulation, are thus an important factor for the development of dust storms near the cap edges. Three-dimensional numerical modelling at mesoscales (Toigo et al., 2002) demonstrated that such winds, generated by the strong thermal contrasts that exist along the edges of the polar caps, are sufficient to initiate dust lifting over quite large areas.

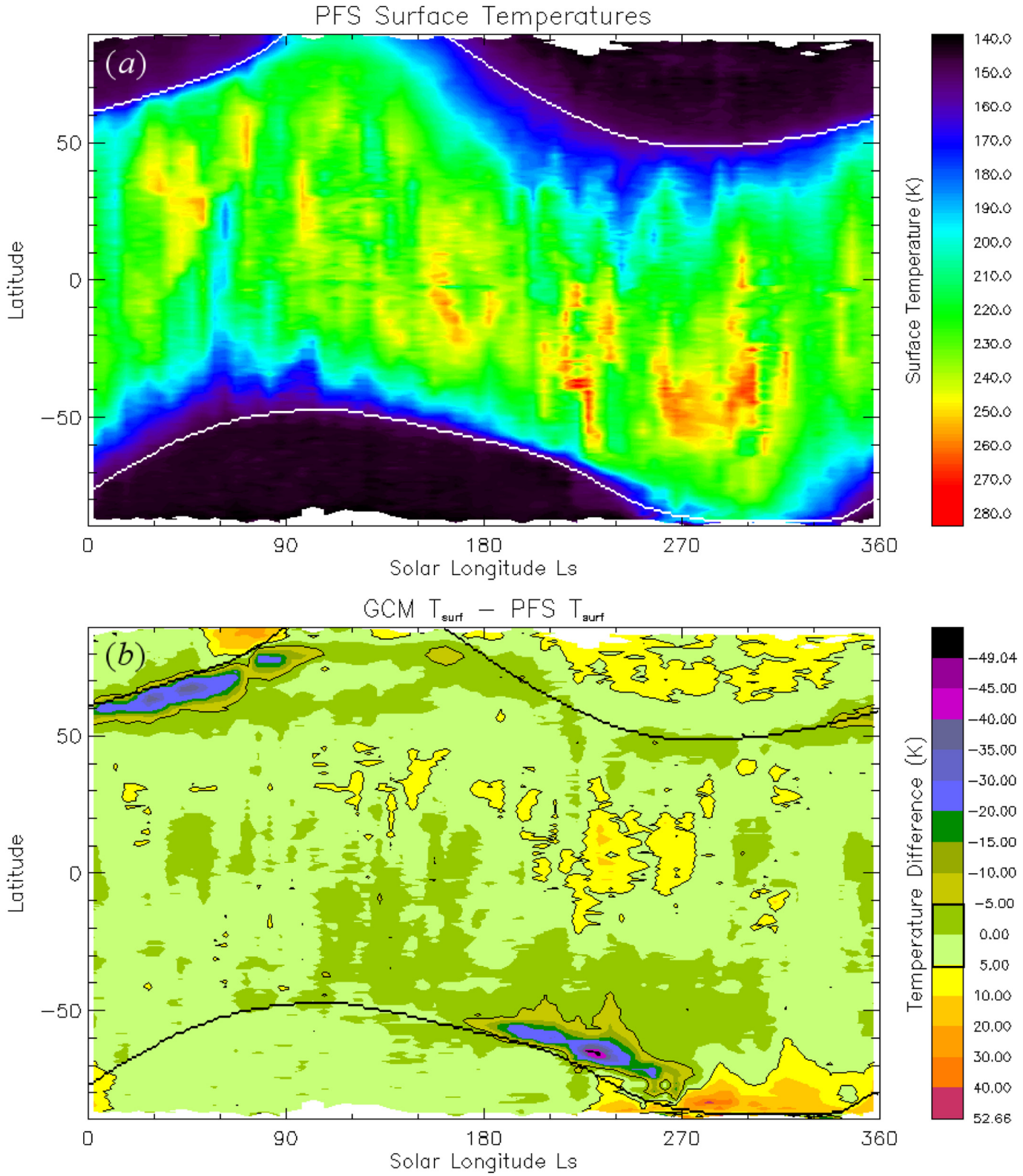


**Fig. 4.** (a) Seasonal variation of zonal-mean surface temperatures measured by PFS. (b) Difference between surface temperatures predicted by the LMD GCM (MCD v5.2) and measured by PFS. Contours mark areas where the difference is larger than ± 5 K. The black curve shows the climatological latitude of the seasonal $CO_2$ polar cap edges (Titus, 2005; Titus and Cushing, 2014). (For interpretation of the references to colour in this figure legend, the reader is referred to the web version of this article.)

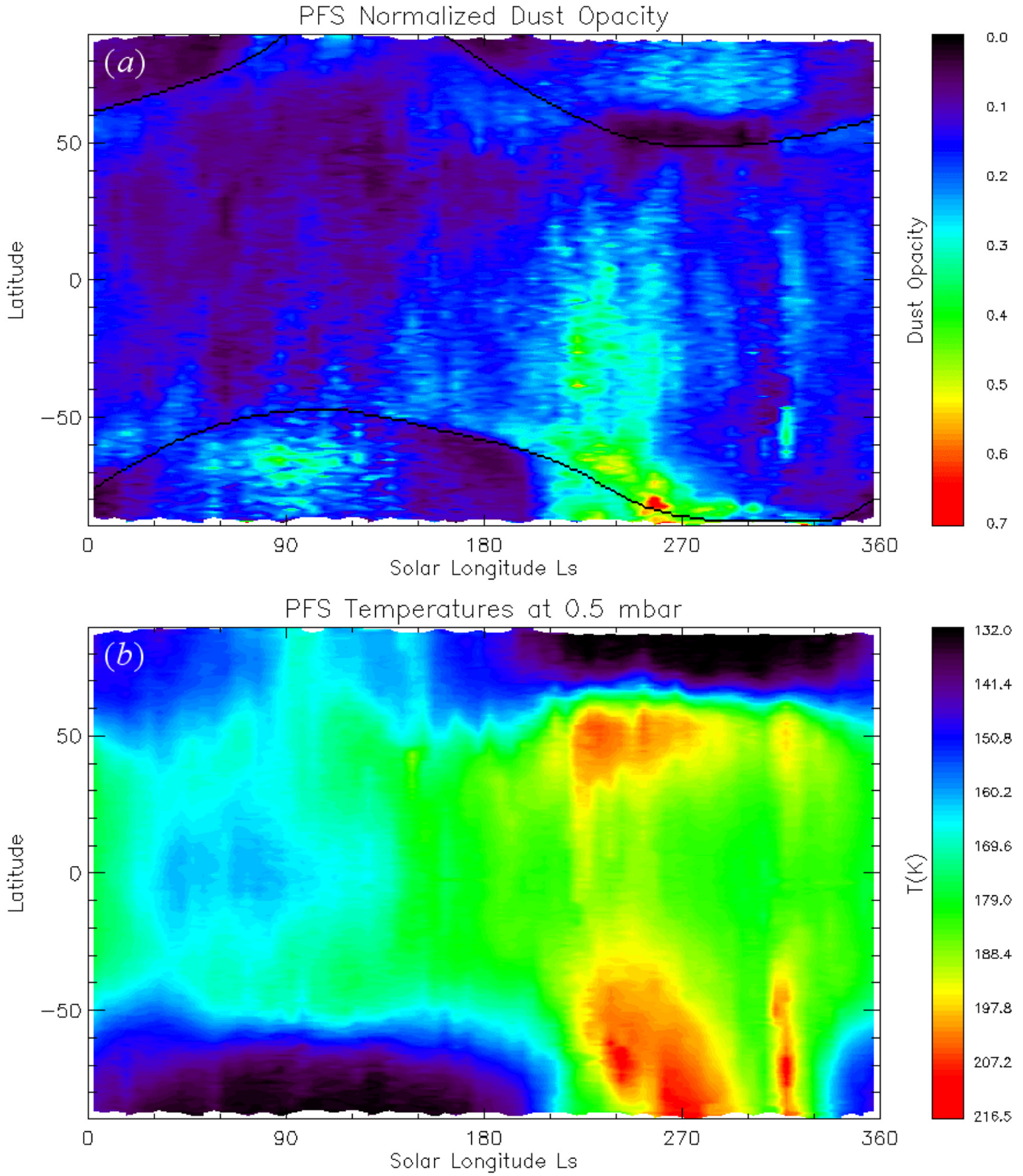


**Fig. 5.** (a) Seasonal and latitudinal variation of zonal-mean dust opacity observed by PFS. Data collected from all observed Martian years (except MY 28) were binned in 5° Ls × 1° latitude bins and normalized to a reference pressure level of 6.1 mbar. The black curve shows the climatological latitude of the seasonal $CO_2$ polar cap edges (Titus, 2005; Titus and Cushing, 2014). Note the continuous dust activity at the edges of the seasonal caps throughout the whole year in both hemispheres, and the development of strong, regional dust storms at high southern latitudes in the 210–270° Ls seasonal range. Note also the extremely dust-clear atmosphere in the northern mid-latitudes (45–60° N latitude) around the winter solstice (Ls = 240–300° Ls) consistently observed every Martian year. The apparent large opacity observed around the winter solstices in both polar regions is actually due to the presence of $CO_2$ ice clouds. (b) PFS zonal-mean temperature structure at 50 Pa (~25 km). See text for more details.

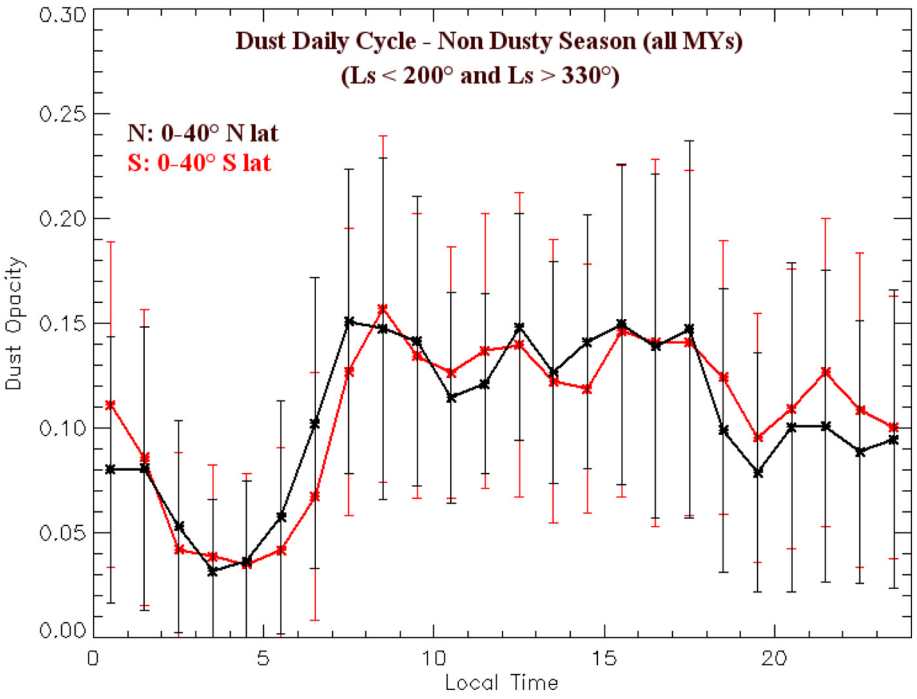


**Fig. 6.** Daily variation of dust opacity during non-dusty seasons, for the indicated seasonal and latitudinal ranges. The "error bars" represent the standard deviation of each averaged value and provide indication of the observed zonal, meridional, and interannual variations. See text for more details. (For interpretation of the references to colour in this figure legend, the reader is referred to the web version of this article.)

Strong regional dust storms occur at high southern latitudes, and particularly in the 210–270° Ls seasonal range, when significant amount of dust is observed every Martian year by PFS from the south pole up to ~30° N (Figs. 1 and 5a). The largest zonally-averaged column-integrated opacities (up to ~0.8) are consistently observed between the perihelion (Ls = 251°) and the southern summer solstice (Ls = 270°) between 70° S and 90° S latitude. Short regional-scale dust events in the southern hemisphere are also observed between 305 and 320° Ls. Although they repeat every Martian year and can extend from −70° to 20° N latitude, these events are generally weak, resulting in typical zonally-average opacities around 0.2–0.3, and never exceeding 0.4. As it is lifted up above the boundary layer, the radiatively active dust absorbs the incident solar radiation and rapidly warms the relatively cool middle atmosphere. This effect is clearly visible in Fig. 5b, where the zonal mean temperatures at 0.5 mbar emphasize the overall impact of dust events on the atmosphere. Increased atmospheric temperatures are also observed in the northern hemisphere, typically around 50° N, in correspondence of the major dust events, due to an intensification of the Hadley circulation driven by dust heating in the southern hemisphere and enhancement of the global thermal tides (Zurek, 1986; Wilson, 1997; Guzewich et al., 2014) as well as the direct dust-driven southern hemisphere heating. The impact of dust on the atmospheric temperatures proved to be a powerful tool to identify and categorize the regional-scale dust events on Mars. Kass et al. (2016) examined the zonal-mean binned temperatures at 0.5 mbar and defined regional-scale storms as events where the temperature exceeds 200 K. These authors identified three major dust-driven warming events in the daytime MCS observations that repeated every Martian year in the absence of global dust storms. Although the starting and ending dates, specific regions and peak heating of the storms vary somewhat from year to year, they always occur in the same order and at similar seasons, and can be recognized in PFS dust and temperature retrievals shown in Fig. 5. All three are regional-scale events with significant warming at all longitudes at the peak of each storm and are labelled in seasonal order A, B, and C. They were described as follows (Kass et al., 2016): the "A storm" is a regional-scale or planet-encircling southern hemisphere dust event occurring at most southern latitudes. It tends to initiate around middle southern spring and has a moderate duration, typically in the 205°–240° Ls range, always over by the southern summer solstice. The "B storm" is a stronger southern polar event which typically starts around perihelion and reaches its peak between the perihelion and the southern summer solstice (Fig. 5a). PFS observations show that the end of the A-type dust activity cannot be clearly defined as these mid-latitudes storms merge with "B storms" originating in the south polar region, especially in the 240°–260° Ls seasonal range (Fig. 5; see also Wolkenberg et al., 2018). The "C storms" are either regional-scale or planet encircling southern hemisphere dust events, except they are very short, mostly occurring between 305°–320°Ls, and are also clearly visible in PFS retrievals in Fig. 5.

Douté et al. (2014) proposed hypothesis regarding the origin of the strong aerosol activity observed in the southern polar region. Simulations of the Martian surface-atmosphere dynamics at mesoscales were used to reproduce observations of the southern seasonal ice regression by several instruments. Two mechanisms were proposed to play a major role for lifting and transporting dust particles, and creating dust events or storms: i) Night-time katabatic winds, which are efficient at locations where a favourable combination of frozen terrains and topography exists and are thought to be the main responsible for the A-type storm events in the 220–255° Ls seasonal range; ii) daytime mesoscale thermal circulation at the edge of the cap (cap-winds), which requires a sharp thermal boundary of regional proportion, and is particularly strong when the defrosting area is sufficiently narrow. The cap winds and the smaller-scale thermal circulation due to the high thermal contrasts associated to segregated terrains in the south polar cap around the perihelion are particularly strong around 250°–270° Ls (Douté et al., 2014), and thus the combination of the two mechanisms might play a role in the development of B-type storm events.

## 4. Daily cycles of dust and ice

PFS retrievals presented here allow for the first time the complete characterization of how dust and ice cloud optical depths vary throughout the day on Mars. Exploiting the non-Sun-synchronous nature of Mars Express orbit, PFS has performed observations of the Martian atmosphere at all local times. In the next three sub-Sections we will present the variation of dust opacity as a function of local time during non-dusty seasons, as well as the daily cycle of ice opacity observed in the aphelion cloud belt, and an assessment of the diurnal

variation of the North and South polar hoods.

### 4.1. Dust daily cycle in non-dusty seasons

Mean values of dust opacity during non-dusty seasons (Ls < 200° and Ls > 330°) are presented in Fig. 6 as a function of local time. Column-integrated dust opacity retrieved by PFS in the various Martian years is averaged in one-hour bins of local time, separately for the northern (0–40° N) and the southern (0–40° S) hemispheres. The different local-time bins have uniform spatial and seasonal sampling. The "error bars" in Fig. 6 represent the standard deviation of each averaged value and provide indication of the combined zonal, meridional, and interannual variation. In both hemispheres, the mean dust opacity shows a clear and similar daily cycle. Dayside mean opacity (7 AM–5 PM) shows near constant values ranging between 0.12 and 0.15, in agreement with previous observations at 2–3 PM during non-dusty seasons. The opacity decreases as the sunset approaches (5–6 PM) and a relative minimum is observed in both hemispheres between 7 and 8 PM. Then, night-time average values around 0.1 are observed up to midnight. After midnight, we consistently observe a rapid decrease of dust opacity. The minimum opacity values are registered in early-morning hours, between 3 AM and 5 AM, when the average column opacity is around 0.03–0.04. As the dawn approaches (5–6 AM), a rapid increase of dust opacity is observed until 7–9 AM, when the mean dayside abundance of suspended Martian dust is restored (Fig. 6). The complete daily cycle of suspended dust in non-stormy seasons described above could not be characterized by any of the previous missions due to limited LT coverage.

The amplitude of daily variability in dust opacity observed by PFS requires injection of dust above the PBL every day in the morning hours (7–9 AM) as well as removal of dust in the nighttime hours, especially in early morning (from midnight to 3–4 AM). Strong diurnal variation of suspended dust on Mars was also observed by MCS (Heavens et al., 2014). These authors reported significant increases of density-scaled opacities on the dayside (3 PM) relative to the nightside (3 AM). We note here that the two local times observed by MCS basically correspond to the time of the day when maxima and minima values of dust opacities are observed by PFS (Fig. 6). The relatively weak longitudinal variability in the spatial distribution of detached dust layers observed by MCS implies that at least one of the injection processes involved is independent of large-scale topography (Heavens et al., 2014). Moreover, the rapid increase of dust opacity observed by PFS soon after the sunrise suggests processes driven by solar heating. Near-surface wind stress (NSWS), saltation, and dust devils are the main mechanisms responsible for dust lifting on Mars (Mulholland et al., 2015; Chapman et al., 2017). NSWS can lift a significant amount of dust in the atmosphere and it is thought to play the dominant role in the initiation of regional and global dust storms (Newman et al., 2002; Strausberg et al., 2005; Kahre et al., 2006; Basu et al., 2006; Wilson, 2011). However, Martian surface winds speeds are thought to be too low to lift micron-sized dust particles directly. Instead, lifting is believed to proceed via saltation, whereby larger particles (a few tens of microns) are partially lifted and fall shortly after entering into atmospheric suspension. On returning to the surface, they collide with smaller particles, sending them into suspension. The wind stress is the shear stress exerted by the wind on the surface and is affected by the wind speed that, in turn, is caused by air moving from high pressure to low pressure, usually due to changes in temperature. For this reason, NSWS is typically larger around the terminator and in the morning hours, when large temperature gradients occur on the surface. Transient convective vortices known as 'dust devils' provide the other main means for dust to enter the atmosphere. The dust devil parameterisation in use in most Mars GCMs results in a high level of dust devil activity during morning hours (Chapman et al., 2017). Apparently, the diurnal variation in dust devil activity is governed by near-surface wind speeds, rather than the activity simply being governed by the availability of heat at the planet's surface. As a result, large areas of the Martian surface experience dust devil activity during the morning (Chapman et al., 2017). In addition, Spiga et al. (2013) used mesoscale modelling of the Martian atmosphere to predict that "rocket dust storm" convection, which is fed by the absorption of incoming sunlight by dust particles, should be most intense during the non-dusty seasons.

On the other hand, the rapid dust removal consistently observed by PFS in early morning suggests that sedimentation is not the dominant process. Once suspended, dust particles will slowly fall to the ground under the influence of gravity, as their density is greater than the atmospheric density. Settling velocity increases with particle size, with sedimentation timescales varying from hours for large (> 50 μm) particles to days and months for small particles, depending also on their altitude. Dust devils may be responsible for lifting particles of all sizes into the atmosphere, as the vortex threshold speed for such an injection appears to be relatively independent of particle size (Neubauer, 1966; Greeley et al., 1981; Cantor et al., 2001). However, the effective radius of dust particles on Mars ranges, on average, from 1.5 to 1.7 μm. Thus, sedimentation alone would require velocities much larger than the $\sim 0.01\ m\ s^{-1}$ estimated by for dust particles of 1–2 μm radius at 0.5–1.0 mbar (Kahre et al., 2008) to explain the rapid decrease of dust opacity observed by PFS in early morning. Among the possible mechanisms, diurnal tides and coating/scavenging of dust particles by water ice clouds may play a role. GCM simulations indicate that the strong, vertically propagating thermal tides on Mars could efficiently clear dust between 3 PM and 3 AM local solar time (Heavens et al., 2014). We note that this temporal interval corresponds well to that of the daily dust removal observed by PFS. In particular, diurnal tide can generate downwelling vertical velocities of $0.2–0.3\ m\ s^{-1}$ at 0.5–1 mbar in the early morning hours. Such large velocities last for about 4 h (Heavens et al., 2014), which is just the duration of the rapid decrease of opacity observed by PFS between midnight and 3–4 AM (Fig. 6). Coating and scavenging of dust particles by water ice clouds might also contribute to the observed daily reduction of dust opacity, and as a possible mechanism of dust removal. The mineral dust is known to act as good cloud condensation nuclei. Dust scavenging by cloud ice can both limit the vertical extent of dust, capping the dust distribution around the height of the ice clouds, and efficiently remove dust, as the particles involved in cloud formation can be subjected to the faster sedimentation that applies to (larger) ice particles (Navarro et al., 2014). However, an explanation involving a cycle of scavenging and lifting on a daily basis does not seem very likely given the timescales involved. If ice is involved, the apparent reduction of suspended dust observed by PFS in early morning may result from daily formation and sublimation of an icy coating onto the dust particles, which can efficiently suppress their spectral signature (Toigo and Richardson, 2000). The condensation-sublimation daily cycle seems more prone than the slow scavenging process at creating dust opacity changes over a few-hour timeframe. PFS observations of the ACB ice opacity as a function of local time for the seasonal range 50–140° Ls are discussed below and shown in Fig. 7. The comparison of dust and ice daily cycles observed by PFS provides support to a role for water ice. Indeed, the time intervals when low dust opacity is observed correspond well with those when large ice opacities are observed (LT < 7 AM and LT > 6 PM; Figs. 6 and 7). Coating, capping and faster sedimentation of dust due to ice may thus contribute to explain the daily dust removal observed by PFS. The association of intense dust removal with cloudy tropical regions observed by MCS also supports this hypothesis (Heavens et al., 2014). An in-depth analysis of PFS water ice and dust opacity datasets will help to address the role of the ice clouds in the daily dust cycle.

### 4.2. Ice daily cycle observed in the ACB

Water ice clouds are strictly associated with water cycle on Mars and its atmospheric circulation (Montmessin et al., 2004; Mateshvili et al., 2009). They occur in different forms including topographically

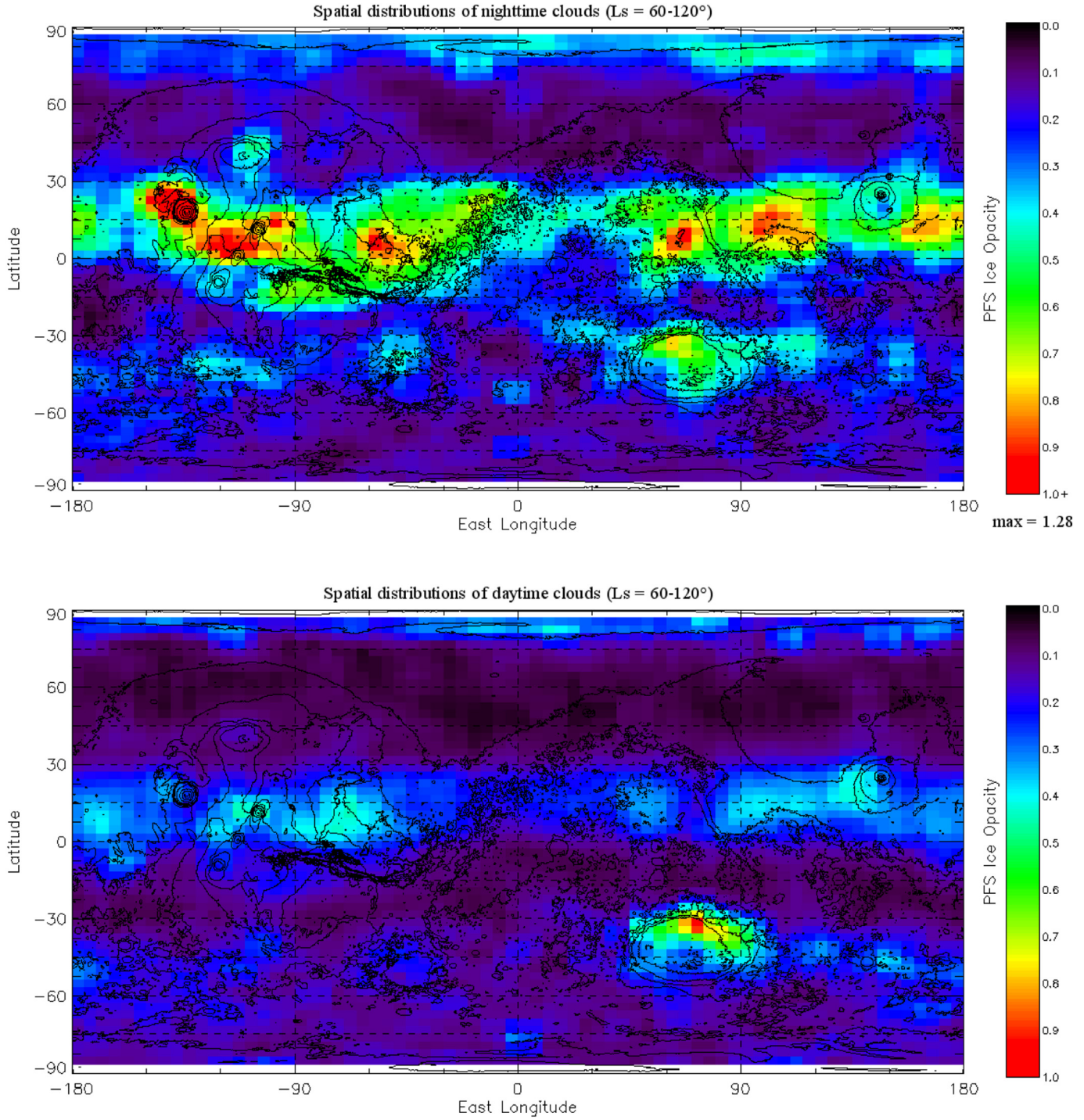


**Fig. 7.** Spatial distributions of (top) nighttime (5 PM ≤ LT ≤ 7 AM) and (bottom) daytime (8 AM ≤ LT ≤ 4 PM) ice clouds in the aphelion cloud belt for the seasonal range indicated. PFS data are binned in 5° lon × 3° lat bins. Black contours are topography from MOLA between −8 km and 20 km altitude (for altitude steps of 2 km) with respect to mars aeroid. (For interpretation of the references to colour in this figure legend, the reader is referred to the web version of this article.)

induced clouds, ground fogs, vast polar hoods, and a low-latitude belt of clouds that activates during the aphelion season between Ls = 40°–140°. Because water ice clouds form by condensation of water vapour, relatively small changes in atmospheric temperature can cause clouds to form or sublimate quickly. As a consequence, large changes in water ice cloud optical depth are expected to occur over the course of a day. Although previous works reported significant diurnal variation of ice opacity, a complete characterization of how cloud optical depths vary throughout the day is not yet available due to the sparse coverage of local time by previous observations. PFS observations of ice opacity presented here can help to fill this gap, by providing full daily cycles of water ice opacity and reconciling the previous results.

In Fig. 7 we present the spatial distribution of nighttime and daytime ice clouds in the aphelion cloud belt as observed by PFS. Data collected from all observed Martian years in the seasonal range Ls = 60°–120° are binned in 5° longitude × 3° latitude bins. The ACB mainly extends from 10° S to 30° N latitude over most of the longitudes, although localized clouds are also observed, especially during nighttime, over Alba Mons (40.5° N, 105° W) and at southern mid-latitudes, over the northern flanks of Hellas and Argyre basins and south of the

steep scarp of Claritas Fosse, between Icaria Fossae and Icaria Planum (43° S and 100–130° W) (Fig. 7). Two distinct large areas of increased water ice opacity are found in the eastern and in the western hemispheres. These areas extend from west of Olympus Mons (150° W) to about 0° W, including Valles Marineris, in the western hemisphere, and from ~30° E to ~195° E in the eastern one. The largest opacities (~1 and up to 1.28) occur over specific regions of elevated terrains and high topographic variation. The ice cloud formation is primarily controlled by thermal tides. Numerical modelling suggests that the tides are strongly influenced by topography and thus water ice clouds are found near the topographic features (Hinson and Wilson, 2004). In the western hemisphere, the thickest clouds are observed over Olympus Mons and the Tharsis volcanoes, as well as over the south-west edges of Chryse Planitia (10° N, 50 W). In the eastern hemispheres, the largest opacities appear over Syrtis Major Planum (10° N, 70° E), along the dichotomy west of Isidis Planitia (15° N, 115° E), and over Elysium Planitia (15° N, 165° E). The daytime and nighttime spatial patterns of ice clouds shown in Fig. 7 are in good qualitative agreement with TES daytime (Smith, 2004) and nighttime (Pankine et al., 2013) observations of the ACB. However, PFS ice opacity is consistently larger than that retrieved by TES. PFS retrieval includes the effect of scattering by aerosols in the infrared. As explained by Smith (2004), the opacity derived from TES measurements does not represent the total opacity of the clouds. By neglecting infrared scattering in their radiative transfer model, the TES retrievals represent extinction due to cloud absorption and/or emission. Noteworthy, the quantitative agreement between TES and PFS is achieved after applying a scaling factor roughly equal to 1.5 to TES values, which is necessary to determine the true ice extinction (Smith, 2004). Spatial patterns derived from MOLA reflectivity (Neumann and Wilson, 2006) and from analyses of TES-derived nighttime surface temperatures anomalies (Wilson et al., 2007), and predicted by GCM simulations (Richardson et al., 2002; Hinson and Wilson, 2004) are also consistent with the PFS spatial maps shown in Fig. 7.

With the exception of those observed over the northern rim of the Hellas basin, the nighttime clouds exhibit larger optical depths and spatial extension compared to the daytime water ice clouds (Fig. 7), which confirms that ice clouds are subject to significant local time variation. Past observation also provided support to this conclusion. Pankine et al. (2013) reported larger ice cloud opacity and spatial coverage during nighttime, and THEMIS retrievals of water ice cloud optical depth taken at ~5:00 PM had higher values than retrievals from contemporaneous observations made by TES at ~2:00 PM (Smith, 2009). Finally, by comparing the spatial patterns of MOLA absorptions with the differences between observed and modelled nighttime surface temperatures, Wilson et al. (2007) concluded that nighttime water ice cloud are thicker and more extensive than daytime clouds in the ACB. The pattern of diurnal change observed by PFS is also consistent with thermal tides controlling cloud formation. The tides are responsible for the formation of strong negative temperature perturbations in the lower atmosphere at night, which further stimulate water ice cloud formation (Hinson and Wilson, 2004).

In Fig. 8 we present the mean value of ice cloud opacity observed by PFS in the aphelion cloud belt as a function of local time. Column-integrated ice opacity retrieved by PFS between 0 and 30° N and 50–140° Ls in different Martian years is averaged in one-hour bins of local time. There is a quite uniform spatial and seasonal sampling in the different local time bins. The “error bars” in Fig. 8 represent the standard deviation of each averaged value and provide indication of the combined zonal, meridional and interannual variation. The observed daily cycle of ice opacity shows a nearly symmetric behaviour around noon, when the minimum of opacity is observed. The mean ice opacity increases almost linearly from midnight, when a value of 0.4 is observed, to 7 AM, when it peaks to a value of ~0.6. The cloud optical depth then rapidly decreases during late morning to a minimum of 0.2 around local noon and increases again during early to mid-afternoon to reach a maximum value of 0.6 around 6 PM, similar to that observed in the morning. Then, the ice opacity decreases almost linearly from late afternoon until midnight. The complete characterization of the variation of the ACB ice opacity throughout the day described above and presented in Fig. 8 finds a positive echo in several previous observations. Akabane et al. (2002) used Earth-based observations to investigate the diurnal variations of ACB ice clouds and, in good agreement with our results, found maximum optical thickness of 0.6 over Tharsis in the morning, and a minimum of 0.2 around noon. Also, consistently with our results, the ice optical depth was found to decrease in late morning and to increase again in early and mid-afternoon. The observed diurnal variations of morning and afternoon clouds repeated regularly for a long period, at least from late spring to early summer (Akabane et al., 2002). Tamppari et al. (2003) studied the diurnal variability of ACB using the Viking Infrared Thermal Mapper (IRTM) and found water ice cloud optical depth to be minimum at midday, with higher optical depth both in the morning and late afternoon. Finally, as already mentioned, Wilson et al. (2007) found nighttime water ice cloud optical depths to be considerably larger than daytime values, and a similar behaviour was observed by TES and THEMIS (Pankine et al., 2013; Smith, 2009).

The nighttime clouds affect the thermal structure of the atmosphere through their radiative cooling. Elevated temperature inversions were observed over the tropics in Radio Science (RS) MGS measurements (Hinson and Wilson, 2004). With the inclusion of radiatively active water ice clouds, simulations by a Martian GCM can fairly reproduce the temperature inversions observed by RS, which were found to be strictly associated to the presence of water ice clouds (Hinson and Wilson, 2004). Consistently to PFS observations, the model predicts cloud formation during late afternoon, after 5 PM, near the temperature minimum at the base of the strong inversions observed by RS. During the course of the night, these inversions (and the associated water ice clouds) reduce progressively with local time. GCM simulations further suggest that water ice clouds formation is induced by adiabatic cooling during night associated to thermal tides. Indeed, the tides are ultimately responsible for the formation of the strong temperature inversions observed in the lower atmosphere at night, which further stimulate water ice cloud formation (Hinson and Wilson, 2004). As also observed by IRTM (Tamppari et al., 2003), clouds almost disappear around noon due to warm atmospheric temperatures. Ice clouds are also observed to increase in thickness and extent from midday to afternoon (Tamppari et al., 2003), possibly due to increased atmospheric temperatures causing uplifting of dust which then acts as cloud condensation nuclei. The daily cycle of water ice clouds observed by PFS in the ACB may then be interpreted as the result of the i) warm dayside temperatures that prevent part of the water vapour to reach the condensation level; ii) increasing opacity from midday to afternoon due condensation on dust nuclei; and iii) strong nighttime tide-clouds coupling.

### 4.3. Diurnal variation of polar hoods opacity

The diurnal (day vs night) variation of the ice opacity (on a zonally-averaged sense) observed by PFS in the polar hoods is presented in Fig. 9. Data collected from all observed Martian years are averaged binned in 5° Ls × 1° latitude bins for two different ranges of local time, 7 PM ≤ LT ≤ 6 AM (nighttime) and 7 AM ≤ LT ≤ 5 PM (daytime). We observe a different behaviour depending on the region and the season. The nighttime SPH is generally more extended than the daytime one, by about 10° of latitude, although ice clouds over Hellas and Argyre are also observed during daytime throughout the southern fall and winter seasons (see also Fig. 3). As already mentioned, daytime and nighttime winter atmosphere over the South Pole is characterized by relatively low ice opacity, in contrast to what is observed in the NPH. The spring NPH (Ls ≤ 90°) exhibits a similar behaviour, being more extended than the seasonal $CO_2$ polar deposits by, on average, about 10° of latitude during nighttime, while during the day it is mostly confined within the

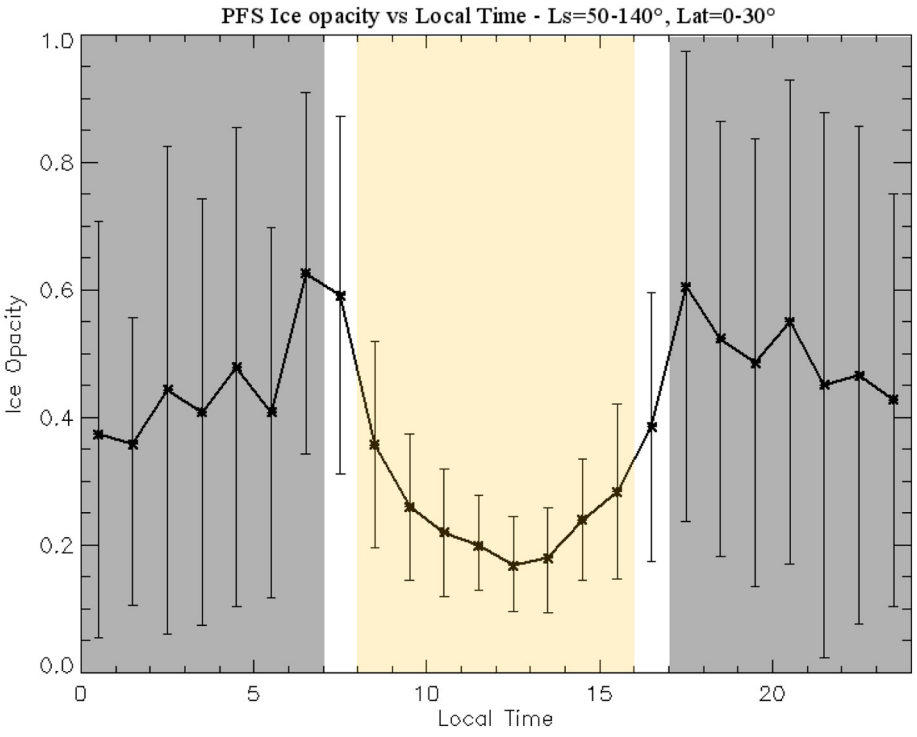


**Fig. 8.** Daily variation of mean water ice opacity observed by PFS in the aphelion cloud belt, for the indicated seasonal and latitudinal ranges. The "error bars" represent the standard deviation of each averaged value and provide indication of the combined zonal, meridional and interannual variation. The grey and the yellowish areas indicate the range of LT selected for the nightside and daytime spatial maps in Fig. 7, respectively. See text for more details. (For interpretation of the references to colour in this figure legend, the reader is referred to the web version of this article.)

seasonal cap edges (Fig. 9). However, the spring NPH shows larger opacities during daylight hours, as most of the water cold-trapped during winter is released as the North polar cap recedes, transported poleward, and then partially re-condenses in the atmosphere and partially redeposits onto the cap (Houben et al., 1997; Montmessin et al., 2004).

## 5. Interannual variability

The temporal coverage of the dataset presented here include six full Martian years, from MY 27 to MY 32, allowing investigation of the interannual variability of mean atmospheric parameters. The mean meridional circulation can be investigated by using zonal averages of atmospheric temperatures, as often applied in model studies. In Fig. 10 we present zonal-mean temperatures in bins of 60° of Solar longitude, from Ls = 180° of MY 29 to Ls = 180° of MY 32. They repeat very similarly on Mars each year, although inter-annual variations ranging from several up to tens of degrees can be observed. Such variations are often, although not exclusively, related to the overall dust content in the Martian atmosphere in the different years. Only daytime temperatures (8 AM ≤ LT ≤ 4 PM) are considered in the various panels of Fig. 10. The orbital resonance of MEx is such that the distribution of local times is essentially the same in the different Martian years. However, some biases could be introduced due to slightly different LT distributions, which could be responsible of some of the differences observed in the various Martian years.

The Hadley cell plays a dominant role in the meridional mean circulation. Its maximum intensity occurs during the solstice seasons (around Ls = 90° and 270°; centre panels in Fig. 10). The ascending branch of the Hadley circulation starts in the summer tropics and transports heat to winter mid latitudes in the descending branch. However, the polar warming, caused by the adiabatic heating of air in the descending branch of the Hadley cell, is much stronger in the northern hemisphere (during the southern summer, Fig. 10b, e, h) than in the southern one (during the northern summer, Fig. 10k, n, q). This is not observed on Earth due to the lower eccentricity of the Earth's orbit and to the presence of oceans, which modulate and mitigate the seasonal oscillations of the surface temperature. Being close to the time of perihelion (Ls = 251°), the Southern-hemisphere summer temperatures (Fig. 10b, e, h) are much larger than the Northern-hemisphere summer ones (Fig. 10k, n, q). As a result, the southern summer Hadley cell is twice more intense than the northern summer counterpart (Richardson and Wilson, 2002). However, in northern summer the Hadley cell descends at ~60° S, that is about 20° of latitude more equatorward than in southern summer, allowing the southern polar vortex to be much broader than that observed in northern winter (central panels of Fig. 10). The region of extremely dust clear air discussed in Section 3.2 (Fig. 5) appears to be located around the low-latitude periphery of the northern polar vortex (black solid lines in Fig. 10b, e, h). The thermal structure around the two equinox periods (Ls = 0° and 180°) is nearly symmetric about the equator (left and right panels of Fig. 10). This is a clear evidence of two main Hadley cells occurring on Mars in these periods (Heavens et al., 2011c).

Over the six years observed by PFS, the strongest regional-scale dust event is observed in MY 29 (middle panel of Fig. 1), when relatively large (> 0.7) zonally-averaged dust opacity is observed, especially at sub-tropical latitudes and during the seasonal range Ls = 220–240°. When compared to, e.g., MY 30 and 31, MY 29 exhibits larger temperatures in the low and mid atmosphere due to the absorption of solar radiation by dust (Fig. 10a, d, and g). The zonal-mean thermal fields in the seasonal range 240–300° Ls for the three years analysed are similar (Fig. 10b, e, and h). However, in this seasonal range, PFS observed a regional increase of dust opacity in MY 31 in two different areas: poleward of ~70° S and between 30 and 40° S latitude (black arrows in Fig. 10h). In these regions, the correlation between dust opacity and atmospheric temperature is particularly evident, with a temperature increase of ~20 K or more around ~1 mbar in correspondence of a dust opacity increase of ~0.2 (black arrows in Fig. 10h). In Fig. 11 we compare the atmospheric temperatures registered during the global dust storm event of MY 28 with those observed over the same seasonal range (240–300° Ls) for a "typical" Martian year (e.g., MY 30), when no global dust storm occurs. The atmosphere is strongly heated up by absorption of solar radiation due to dust, as expected. A net heating is observed for altitudes above ~1 mbar, where the mean atmospheric temperature is up to 28 K warmer than for a typical Martian year (Fig. 11c). These altitudes are just above the height of the peak of dust

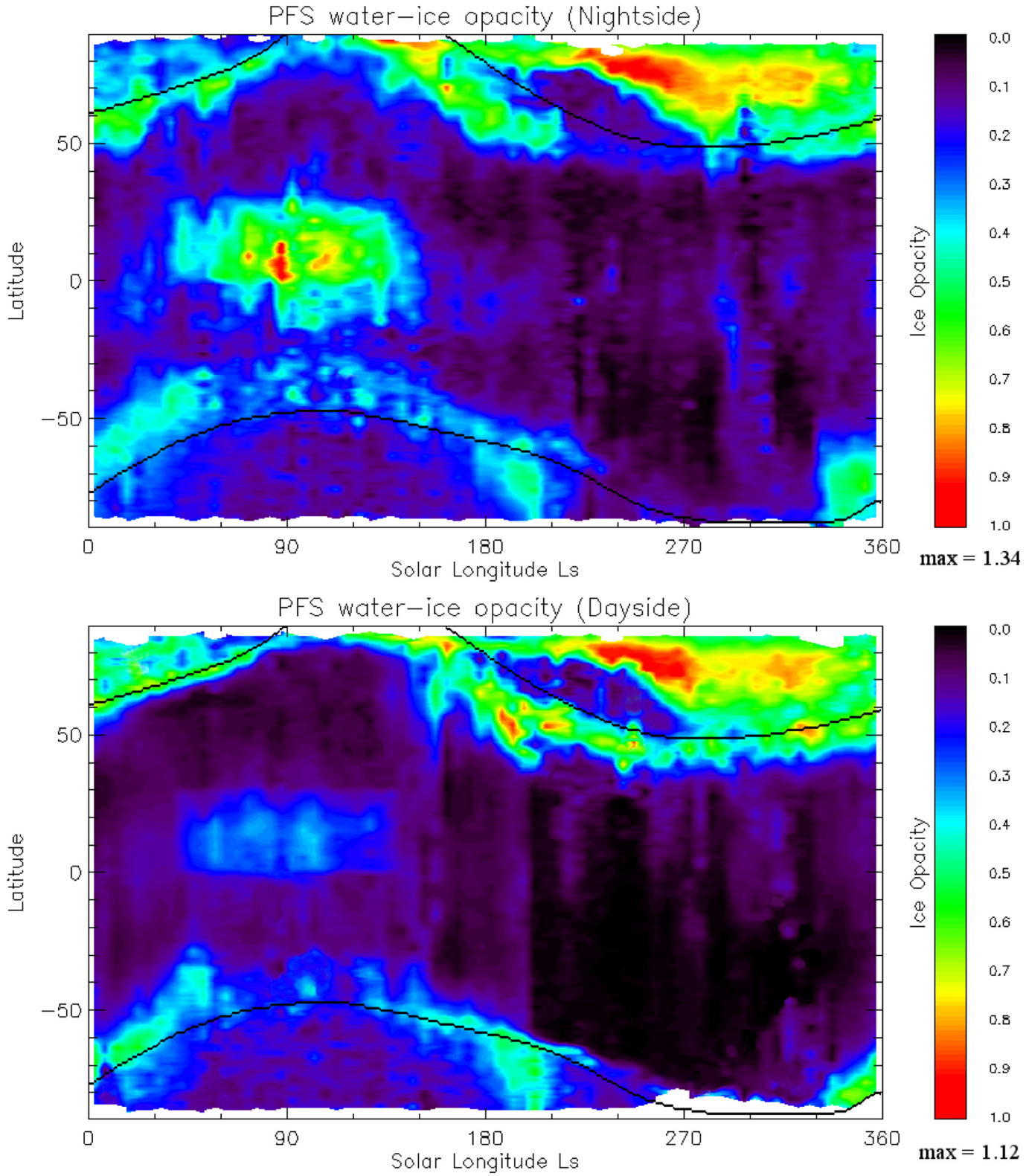


**Fig. 9.** Same as in Fig. 2 but for (top) nighttime (7 PM ≤ LT ≤ 6 AM) and (bottom) daytime (7 AM ≤ LT ≤ 5 PM) hours.
During the fall and winter seasons (Ls ≥ 180°), the NPH exhibits two different behaviours, depending on the latitude. Poleward of the seasonal cap edges, the ice cloud opacity shows little or no diurnal variation. Beyond the cap edges (i.e., at lower latitudes) the NPH shows larger opacity during daytime, possibly due to sublimation of the exposed water ice annulus and subsequent re-condensation in the atmosphere as ice clouds (Wagstaff et al., 2008; Kuzmin et al., 2012) (For interpretation of the references to colour in this figure legend, the reader is referred to the web version of this article.).

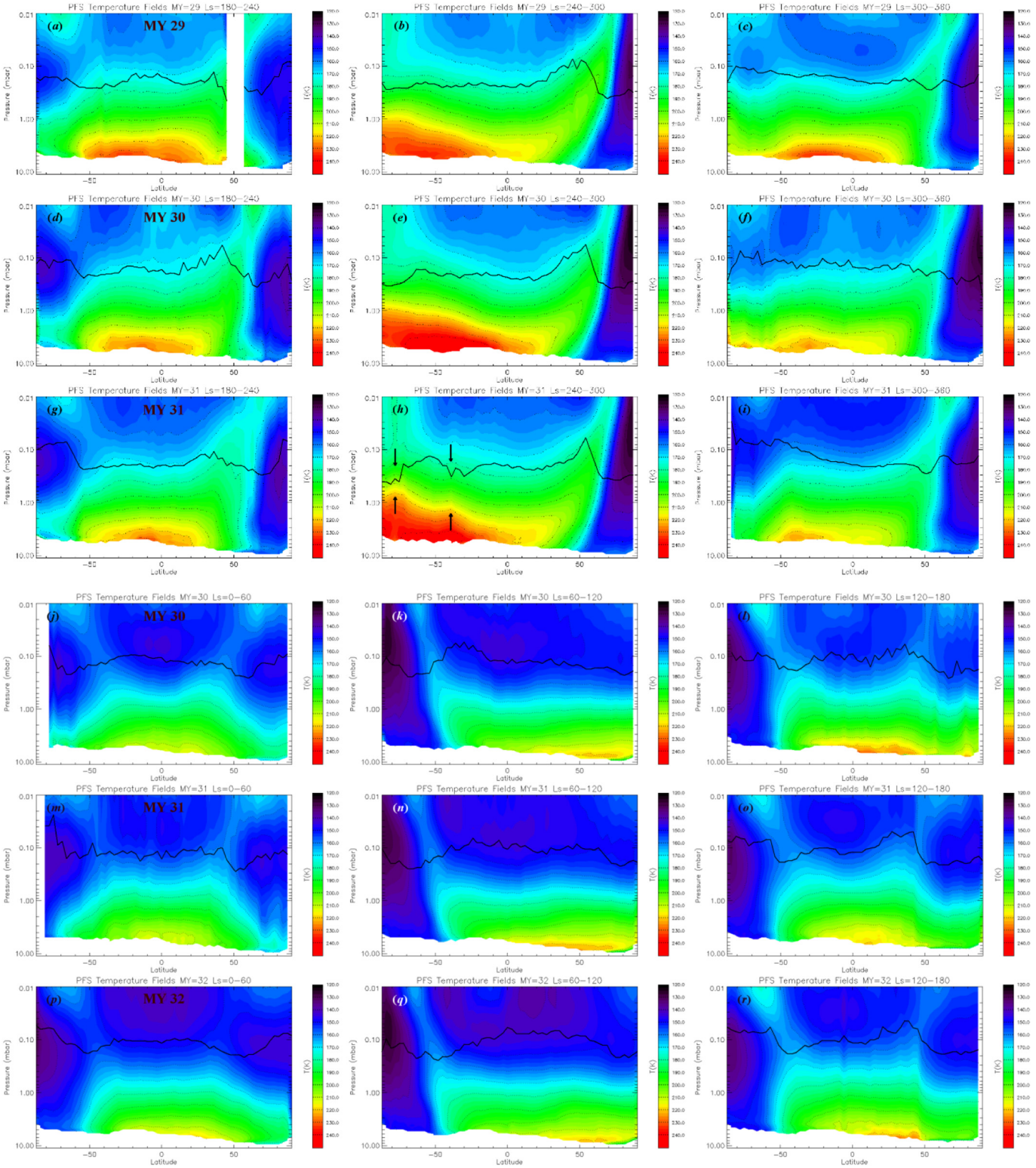


**Fig. 10.** Daytime (8 AM ≤ LT ≤ 4 PM) zonal-mean atmospheric temperatures for bins of 60° Ls and for different Martian years, as indicated. The logarithmic vertical scale is used both for pressure and dust opacity (black solid line). The colour scale is the same in all panels. (For interpretation of the references to colour in this figure legend, the reader is referred to the web version of this article.)

extinction measured by MCS (Heavens et al., 2011a, 2011b; Wolkenberg et al., 2018). However, the infrared radiative cooling rates due to dust cannot be overlooked in the lower altitudes within dusty atmosphere. Especially during a dust storm event, cooling in the infrared regions is comparable to heating due to absorption of the incident solar radiation by dust, and the thermal structure of the atmosphere is determined by the balance between heating and cooling caused by radiative effects of dust. During the global dust storm of MY 28 we observe a net cooling of the lower atmospheric layers of up to 26 K, on a zonally average sense (Fig. 11c). The region (latitude) of maximum cooling corresponds to the region where the largest dust opacity is observed (Fig. 11a). Solar shielding by thick dust layers may

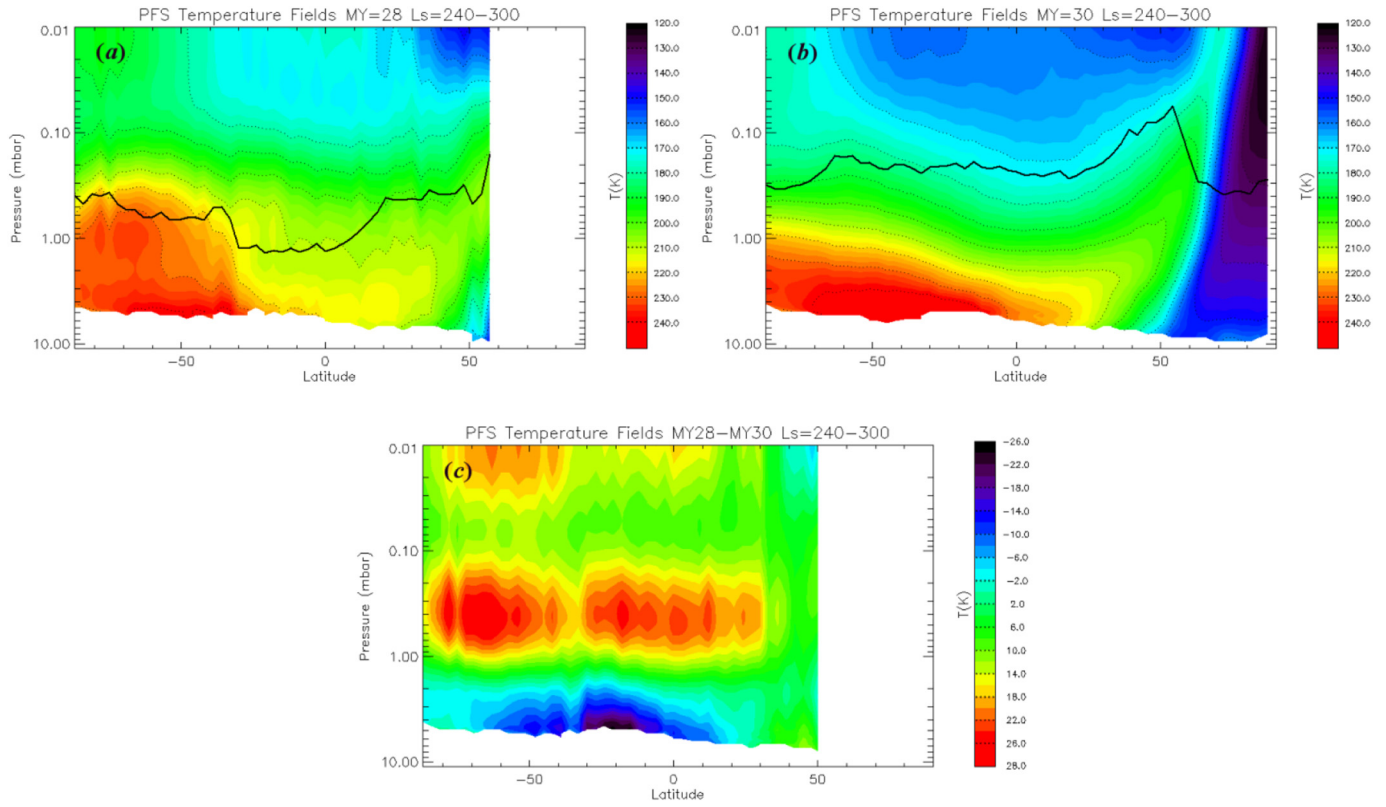


**Fig. 11.** Impact of MY 28 dust storm on daytime (8 AM ≤ LT ≤ 4 PM) atmospheric temperatures. Zonal mean atmospheric temperatures (a) during the global dust storm occurred in MY 28 and (b) for MY 30 for the seasonal range indicated. (c) Difference between (a) and (b). (For interpretation of the references to colour in this figure legend, the reader is referred to the web version of this article.)

also contribute to the cooling of the lower atmospheric layers. Wolkenberg et al. (2018) used temperature vertical profiles and column-integrated dust optical depth retrieved by PFS, as well as dust vertical profiles derived by MCS observations, to investigate the influence of dust on atmospheric temperatures. These authors calculated the cooling and heating rates due to dust in the infrared range (~9 μm) and in the visible range (~0.67 μm), respectively, and consistently observed a significant net heating of the atmospheric layers just above the peak-altitude of dust opacity, due to absorption of the visible solar radiation, and a net cooling in the first two or three atmospheric scale heights, due to radiative cooling. The net heating rate increases with total dust opacities. Even low amount of dust (opacity around 0.15) produces a net heating rate of several degrees Kelvin per day, while relatively high opacities (> ~1.5) can heat the atmospheric layers by 40 K/day or more (Wolkenberg et al., 2018). Such results are consistent with those presented in Figs. 10 and 11 and discussed above.

### 5.1. Aphelion cloud belt

The mean nighttime (5 PM ≤ LT ≤ 7 AM) ice opacity observed in the aphelion cloud belt, averaged for the various years of PFS observations, is shown in Fig. 12. Although it can be observed throughout the northern spring and summer ($L_s$ = 0°–180°), thicker clouds (mean nighttime opacity > 0.2) typically start to form around Ls = 40°. After this solar longitude, the mean opacity progressively increases and reaches a peak of 0.6 or more, on average, between Ls = 90–110°, when

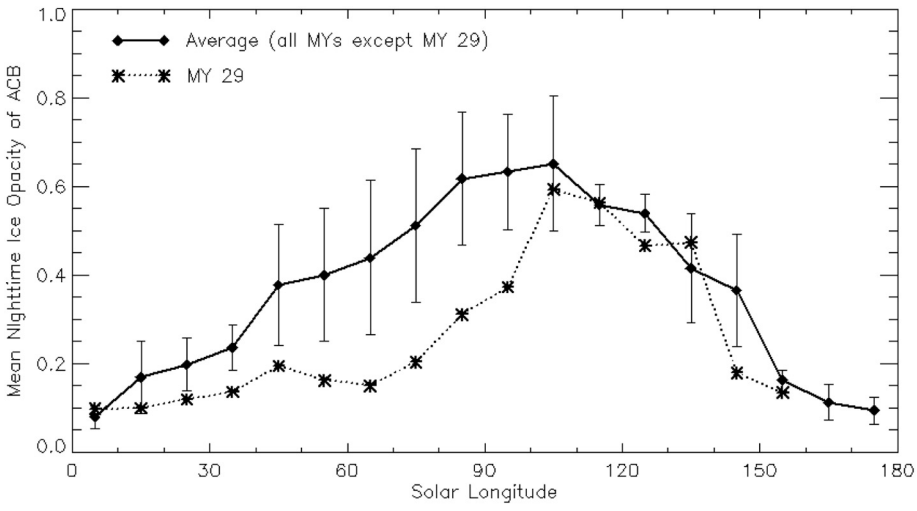


**Fig. 12.** Mean nighttime (5 PM ≤ LT ≤ 7 AM) ice opacity observed by PFS in the aphelion cloud belt for the Martian years indicated. As an indication of the observed interannual variability, the error-bars represent the standard deviation of mean opacity observed in the various Martian years (MY 27 to MY 32). See text for more details.

the larger extension of the ACB is also observed (Fig. 3d). It then gradually dissipates, especially after Ls = 140°, until the end of the summer. As previously reported (Smith, 2004; Smith, 2009), the ACB shows little interannual variability, the values of water ice opacity and the distribution of water ice clouds being very similar from year to year. The largest interannual variability, indicated by the error-bars in Fig. 12, is observed during its formation and expansion phases, that is between 40° and 110° of solar longitude. However, Martian year 29 appears to be an exception. In this year, the formation of thick water ice clouds starts much later than in the other years. Mean nighttime opacities larger than 0.2 are only observed after Ls = 80°. Nevertheless, the maximum value of the mean opacity is consistent with that observed in the other years, and so is the Solar longitude at which it is observed. The regression and dissipation of the ACB observed in MY 29 is also consistent with those of the other Martian years. We don't have an explanation for the different seasonal evolution of the ACB observed in MY 29. The local times sampled in the various MYs are quite uniform and so are the latitudes and longitudes. Moreover, we selected 5 PM ≤ LT ≤ 7 AM. Here, only relatively small variation of the mean water ice opacity with LT is observed (see Fig. 8).

## 6. Summary and conclusions

We presented a new dataset of atmospheric parameters retrieved by the Planetary Fourier Spectrometer (PFS) on Mars Express. Thermal-infrared spectra collected in the first 12 years of operations were used to retrieve atmospheric temperature profiles, surface temperatures, and column-integrated optical depths of dust and water ice. More than 2,500,000 spectra were processed to build this dataset, covering the full range of season, latitude, longitude, and local time, from Ls = 331° of MY 26 (10 January 2004) to Ls = 78° of MY 33 (December 2015). Atmospheric temperatures and aerosols opacity are successfully retrieved in the polar regions, including the polar nights, where most of the peculiar features were observed. By exploiting PFS/MEx capability to perform observations at different local times, the new PFS dataset allowed a complete characterization of how dust and ice cloud optical depths vary throughout the day on Mars. The dataset presented in this paper will be constantly updated as new observations will be acquired by the PFS and new retrievals will be performed. The dataset is available in NetCDF format and can be obtained, on request, from the corresponding author.

### 6.1. Climatology of dust

We investigated the latitudinal and seasonal evolution of dust activity on Mars. A region of extremely dust-clear atmosphere separates the dust in the winter tropics from the aerosols (mainly $CO_2$ ice clouds) in the winter high latitudes. This feature repeats every Martian year and is mainly observed at mid-latitudes (45–60° N) around the northern winter solstice (Ls = 220–310°). It corresponds well with the area of the atmosphere heated primarily by the descending branch of the Hadley circulation and was also observed by TES and MCS. Currently, this feature is not reproduced by any of the GCMs available for Mars.

PFS regularly observes dynamic dust activity near edges of the seasonal caps throughout the year in both hemispheres, induced by thermal gradients resulting from the expansion and regression of the polar caps. Strong regional dust storms occur at high southern latitudes in the 210–270° Ls seasonal range, when significant amount of dust is observed every Martian year by PFS from the south pole up to ~30° N. Type A, B, and C storms as defined by Kass et al. (2016) through daytime MCS observations can be recognized in PFS observations of dust and atmospheric temperatures.

### 6.2. Climatology of water ice

We presented the seasonal and latitudinal variation of water ice cloud optical depth. Previous instruments were unable to confidently retrieve aerosol opacities above the $CO_2$ seasonal caps. This limitation excluded a significant part of the cloud annual cycle, as demonstrated by the PFS observations of the polar hoods. In contrast to what reported by previous analyses of different datasets, the most prominent feature observed by PFS is the seasonal extent, pattern and thickness of the NPH, rather than the ACB. Most of the thickest Martian clouds are observed in the polar hoods. The extent of the polar hoods varies with the season and their boundaries always exceed those of the seasonal $CO_2$ polar caps in either hemispheres. The NPH exhibits larger opacities and always extends to the pole, while the SPH is an optically thinner annular ring that basically follows the climatological latitudes of the seasonal cap edge. The SPH extends up to the pole in two relatively narrow seasonal ranges, 180–205° Ls and 330–360° Ls, when the largest opacities are also observed. The NPH shows peculiar features, observed in detail here for the first time, with characteristic spatial and seasonal patterns that repeat very similarly every Martian year. Large opacities (> 0.5) are always observed at latitudes > 80° N, from the summer solstice (Ls = 90°) until the vernal equinox (Ls = 360°). A region where practically no ice clouds form during the entire northern fall is consistently observed every MY between 170° and 280° Ls. It is always about 60° of solar longitude wide and moves latitudinally towards lower latitudes as the season advances. It is first observed around 170° Ls and 75° N. Then, it gradually extends to lower latitudes with the season, down to ~50° N in the seasonal interval 220–280° Ls. Possible interpretations of this ice-free region include clouds formation controlled by the atmospheric temperature structure; a connection to the descending branch of the Hadley circulation; as well as the partial inability of water vapour to penetrate into the north polar vortex, preventing the clouds to be formed at higher latitudes.

Thick ice clouds are always observed over Hellas basin during most of the northern spring and summer season (from 30° to 150° of solar longitude) and especially along the northern rim of the crater, while ice clouds form over Argyre basin during most of the northern spring. The ACB is observed by the PFS in every Martian year. It reaches peaks in optical depth and extension around Ls = 100°, and gradually dissipates after Ls = 140°.

### 6.3. Daily variation of dust

Mars' climate models are still doing very poorly to create diurnal variation in the dust distribution. PFS observations of the dust daily cycle during non-storm seasons suggest that moderate amount of dust is rapidly lifted in the atmosphere during the 2 or 3 h after the sunrise, and remains suspended for the whole day. Dayside mean opacity shows constant values ranging between 0.12 and 0.15. The atmospheric dust content slowly decreases from the terminator to midnight, and then rapidly reaches its minimum values of ~0.03 in early morning (3–4 AM) in both hemispheres. The daily variability in dust opacity observed by PFS requires injection of dust above the PBL every day, especially in the morning hours (7–9 AM), as well as removal of dust in the nighttime hours, especially from midnight to 3–4 AM. The rapid increase of dust opacity observed by PFS soon after the sunrise suggests processes driven by solar heating. Near-surface wind stress, which is typically larger around the terminator and in the morning hours; intense dust devil activity during the morning; and “rocket dust storm” convection may provide a possible explanation for the rapid increase of dust opacity observed by PFS in morning hours of non-dusty seasons. The rapid dust removal consistently observed by PFS in early morning suggests that processes other than sedimentation dominate the process. The most likely mechanisms are large downwelling vertical velocities generated by diurnal tides and coating/scavenging of dust particles by water ice clouds.

### 6.4. Daily variation of water ice cloud in the ACBs

The ACB mainly extends from 10° S to 30° N latitude over most of the longitudes. The largest opacities (~1 and up to 1.28) occur over specific regions of elevated terrains and high topographic variation. In the western hemisphere, the thickest clouds are observed over Olympus Mons and the Tharsis volcanoes, as well as over the south-west edges of Chryse Planitia (10° N, 50 W). In the eastern hemispheres, the largest opacities appear over Syrtis Major Planum (10° N, 70° E), along the dichotomy west of Isidis Planitia (15° N, 115° E), and over Elysium Planitia (15° N, 165° E). Localized clouds are also consistently observed at northern and southern mid latitudes, especially during nighttime, over Alba Mons, the northern flanks of Hellas and Argyre basins, and south of the steep scarp of Claritas Fosse. With the exception of those observed over the northern rim of the Hellas basin, the nighttime clouds exhibit larger optical depths and spatial extension compared to the daytime water ice clouds.

Because water ice clouds form by condensation of water vapour, relatively small changes in atmospheric temperature can cause clouds to form or sublimate quickly. As a consequence, large changes in water ice cloud optical depth are expected to occur over the course of a day. The daily cycle of ice opacity in the ACB observed by PFS shows a nearly symmetric behaviour around noon, when the minimum of opacity is observed. The mean ice opacity increases almost linearly from midnight (mean value ~0.4) to 7 AM (peak value ~0.6). The clouds optical depth then decreases during late morning to a minimum of 0.2 around local noon, and increases again during early to mid-afternoon to reach a maximum value of 0.6 around 6 PM, similar to that observed in the morning. The daily cycle of water ice clouds observed by PFS in the ACB finds a positive feedback in several previous observations and can be interpreted as the result of several mechanisms, including warm dayside temperatures that prevent part of the water vapour to reach the condensation level; increasing opacity from midday to afternoon due condensation on dust nuclei; strong tide-clouds coupling which further stimulate water ice cloud formation during nightside.

### 6.5. Interannual variability

The temporal coverage of the dataset presented here includes six full Martian years, from MY 27 to MY 32, allowing investigation of the interannual variability of mean atmospheric parameters. Zonal-mean atmospheric temperatures collected in the various Martian years exhibit inter-annual variations, ranging from several up to tens of degrees. Such variations are often, although not exclusively, related to the overall dust content in the Martian atmosphere in the different years. Over the six years observed by PFS, the strongest regional-scale dust event is observed in MY 29, when large ($> 0.7$) zonally-averaged dust opacity is observed, especially at sub-tropical latitudes and during the seasonal range $L_S = 220–240°$. When compared to the other years, MY 29 exhibits larger temperatures in the low and mid atmosphere due to the absorption of solar radiation by dust. During MY 31 PFS observed a regional increase of dust opacity in the South Polar region (poleward of ~70° S) and between 30 and 40° S latitude. In these regions, the correlation between dust opacity and atmospheric temperature is evident, with large increase of atmospheric temperatures (20 K or more) in correspondence of relatively small increase of dust opacity (~0.2).

A global dust storm occurred on Mars in MY 28. During this event, the atmosphere was strongly heated up by absorption of solar radiation due to dust. A net heating is observed for altitudes above ~1 mbar, where the mean atmospheric temperature is ~30 K warmer than for a typical Martian year. However, a net cooling of the lower atmospheric layers of up to 26 K is also observed, demonstrating that the infrared radiative cooling rates due to dust cannot be overlooked in the lower altitudes within dusty atmosphere.

The ACB shows little interannual variability, the values of water ice opacity and distribution of water ice clouds being very similar from year to year. The largest interannual variability is observed during its formation and expansion phases, that is between 40° and 110° of solar longitude. Martian year 29 appears to be an exception. In this year, the formation of thick water ice clouds starts much later (~40° of solar longitude) that in the other years.

The dataset presented here allowed investigation of the current weather and climate on Mars. With unprecedented spatial and temporal coverage and details revealed, this dataset offers new challenges to the GCMs and, at the same time, a new reference for the MYs complementary to those observed by previous instruments. Further analysis and comparison to the available GCMs are needed for a complete interpretation of PFS observations. Current climate models are unable to reproduce the diurnal (TES, MCS and PFS) and daily (PFS) variation of dust and ice content observed on Mars. Comparisons of improved model predictions to PFS observations, as well as assimilation of previously-unavailable dust and ice retrievals in the polar regions and at all local times, will be of invaluable importance to interpret the observations and to understand the processes involved.

## Acknowledgements

This work has been performed under the UPWARDS project. This project has received funding from the European Union's Horizon 2020 research and innovation programme under grant agreement No. 633127. The PFS experiment has been built at the “Istituto di Astrofisica e Planetologia Spaziali” (IAPS) of the “Istituto Nazionale di Astrofisica” (INAF) and is currently funded by the Italian Space Agency (ASI) in the context of the Italian participation to the ESA's Mars Express Mission (grant ASI/INAF n. 2018-2-HH.0). The computational resources used in this research have been supplied by INAF-IAPS through the DataWell project.

The authors would like to thank the two reviewers, Michael Smith and Franck Montmessin, for their valuable comments and suggestions to improve the quality of the paper.

## Appendix A

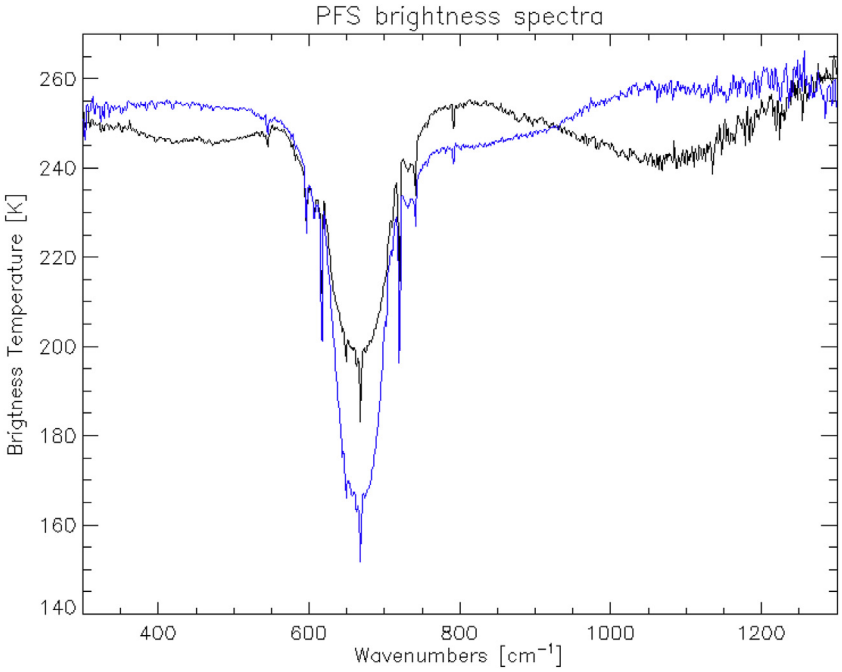


**Fig. A1.** Single PFS brightness spectra recorded over the Aphelion Cloud Belt in MY 27 (blue curve, Ls = 62°, LT = 8 AM, Lat = 1° N, Lon = −83° E) and during the MY 28 Global Dust Storm (black curve, LS = 280°, LT = 11 AM, Lat = 1° N, Lon = 72° E). (For interpretation of the references to colour in this figure legend, the reader is referred to the web version of this article.)

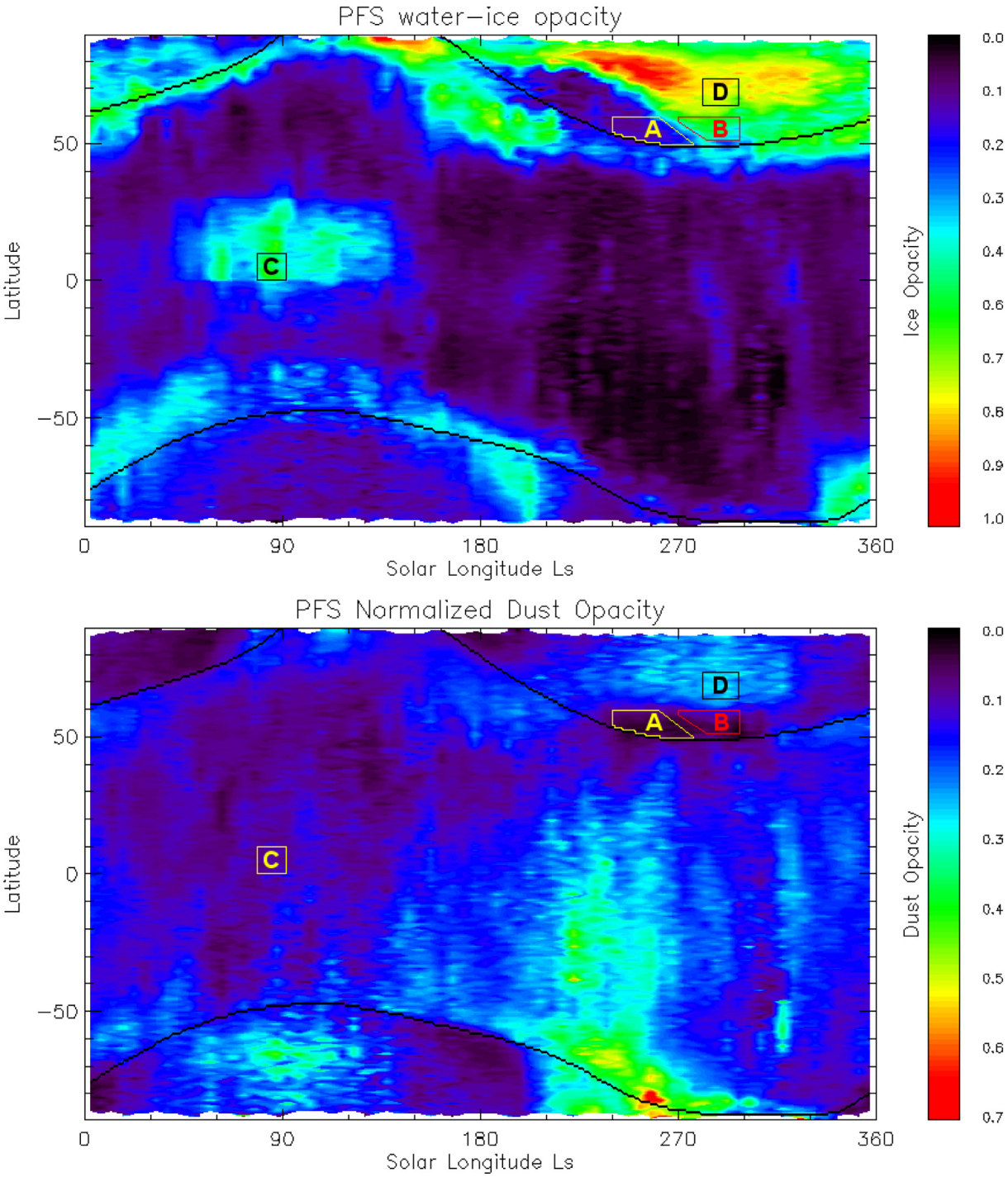


**Fig. A2.** The PFS spectra shown in the next figures are selected within the four regions here defined. Region A: a portion of the "cloud-free" region observed every MY in the northern polar region during the fall season; Region B: North polar hoods; Region C: aphelion cloud belt; Region D: $CO_2$ ice clouds (retrieved as dust). See text for more details. (For interpretation of the references to colour in this figure legend, the reader is referred to the web version of this article.)

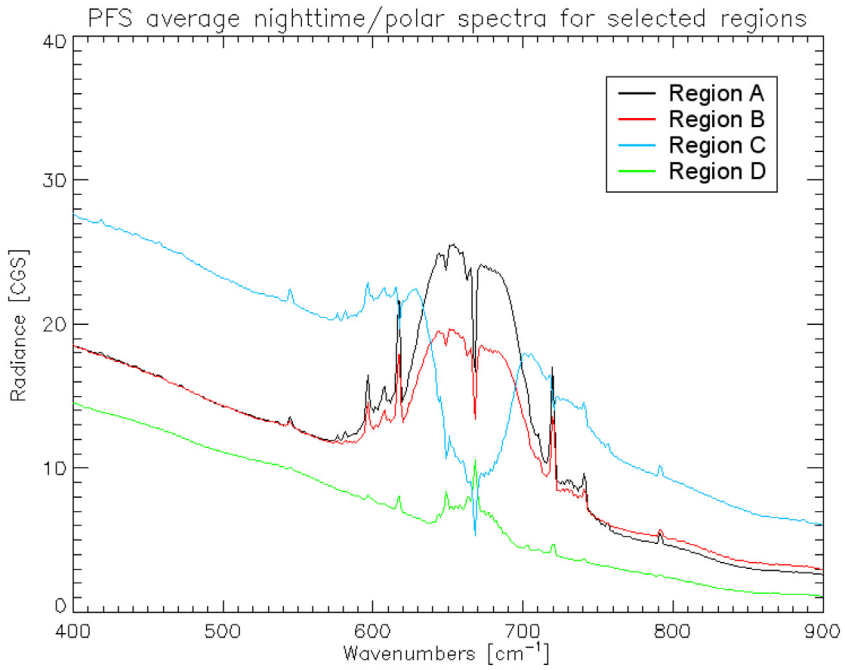


**Fig. A3.** PFS nighttime (7 PM ≤ LT ≤ 6 AM) average spectra in the four regions defined in Fig. A2. (For interpretation of the references to colour in this figure legend, the reader is referred to the web version of this article.)

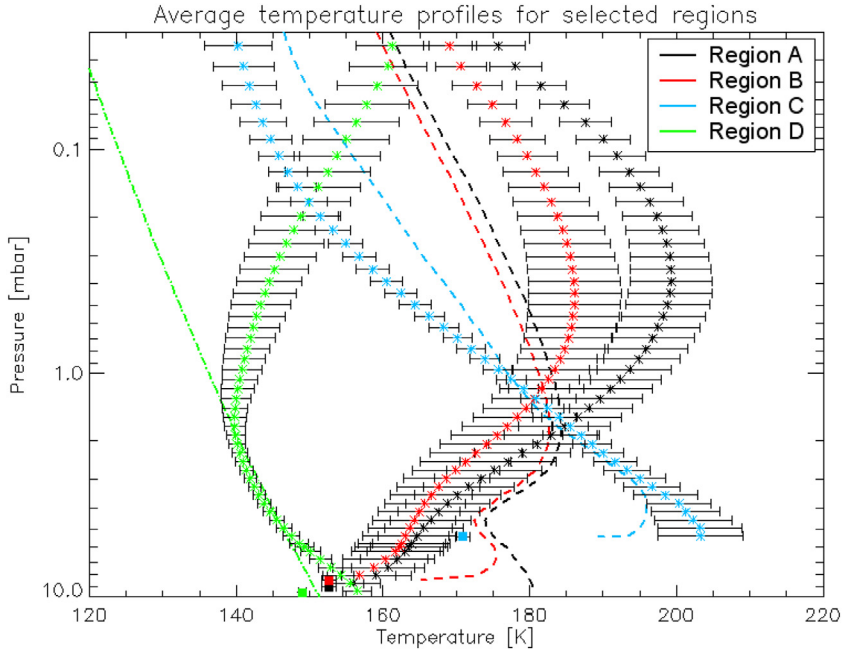


**Fig. A4.** PFS-retrieved average temperature profiles relative to the spectra shown in Fig. A3. 1-σ error bars are also shown. Squares: surface temperatures. Dashed lines: water vapour saturation profiles calculated using the average mixing ratio profiles extracted from MCD v.5.2 for the same geometry as the PFS observations. Green dash-dotted line: $CO_2$ condensation profile for a uniform $CO_2$ mixing ratio of 0.9532. (For interpretation of the references to colour in this figure legend, the reader is referred to the web version of this article.)

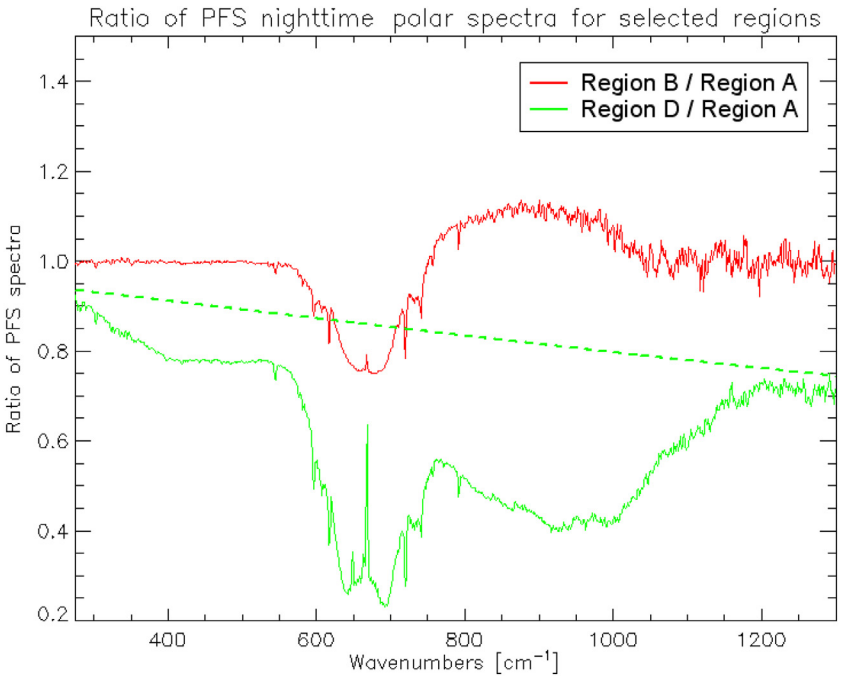


**Fig. A5.** Ratio of PFS polar night spectra collected in different regions. Regions A, B, and D are defined in Fig. A1. The low surface temperatures (due to the presence of $CO_2$ ice on the ground) and the temperature inversions that occur in the polar night atmosphere tend to mask and distort the aerosol spectral features present in the polar night spectra. One way to show such "hidden" features is through the ratio of two PFS polar night spectra: one in a relatively aerosol-free region, and the other with relatively large ice or dust (actually $CO_2$ clouds retrieved as dust, as explained in the text) opacity retrieved. The red curve is the ratio of the PFS average spectrum in region B (north polar hoods) to the average spectrum of region A ("cloud-free" region). The water ice spectral features are seen in "emission", the ice clouds being warmer that the surface temperature (see Fig. A4). The green curve is the ratio of the PFS average spectrum in region D ($CO_2$ ice clouds) to the average spectrum of Region A ("cloud-free" region). The curve shows mixed features of $H_2O$ and $CO_2$ ice. The slope is due to the different surface temperatures in the two spectra (see Figs. A3 and A4). The green dashed line is the ratio of a Planck radiance at $T = 149$ K to a Planck radiance at 152.6 K, i.e., the average surface temperatures for region D and region A, respectively. (For interpretation of the references to colour in this figure legend, the reader is referred to the web version of this article.)

## References


Akabane, T., Iwasaki, K., Saito, Y., Narumi, Y., 1993. Martian late northern winter polar hood opacities and non-visibility of a surface cap: 1975 and 1990 observations. Astron. Astrophys. 277, 302–308.

Akabane, T., Nakakushi, T., Iwasaki, K., Larson, S.M., 2002. Diurnal variation of Martian water-ice clouds in Tharsis region of the low latitude cloud belt: observations in 1995–1999 apparitions. A&A 384, 678–688.

Bapst, J., Bandfield, J.L., Wood, S.E., 2015. Hemispheric asymmetry in Martian seasonal surface water ice from MGS TES. Icarus 260, 396–408.

Barnes, J.R., Haberle, R.M., Wilson, R.J., Lewis, S.R., Murphy, J.R., Read, P.L., 2017. The global circulation. In: Haberle, R.M., Clancy, R.T., Forget, F., Smith, M.D., Zurek, R.W. (Eds.), The Atmosphere and Climate of Mars. Cambridge University Press, Cambridge, UK, pp. 229–294.

Basu, S., Wilson, J., Richardson, M.I., Ingersoll, A., 2006. Simulation of spontaneous and variable global dust storms with the GFDL mars GCM. J. Geophys. Res. 111 (9), E09004. https://doi.org/10.1029/2005JE002660.

Benson, J.L., James, P.B., Cantor, B.A., Remigio, R., 2006. Interannual variability of water ice clouds over major Martian volcanoes observed by MOC. Icarus 184, 365–371.

Benson, J.L., Kass, D.M., Kleinböhl, A., McCleese, D.J., Schofield, J.T., Taylor, F.W., 2010. Mars' south polar hood as observed by the Mars Climate Sounder. J. Geophys. Res. 115, E12015. https://doi.org/10.1029/2009JE003554.

Benson, J.L., Kass, D.M., Kleinböhl, A., 2011. Mars' north polar hood as observed by the Mars Climate Sounder. J. Geophys. Res. 116, E03008. https://doi.org/10.1029/2010JE003693.

Bohren, C.F., Huffman, D.R., 1983. Absorption and Scattering of Light by Small Particles. John Wiley, New York.

Cantor, B.A., James, P.B., Caplinger, M., Wolff, M.J., 2001. Martian dust storms: 1999 Mars orbiter camera observations. J. Geophys. Res. 106 (E10), 23653–23687.

Cantor, B.A., Malin, M., Edgett, K.S., 2002. Multiyear Mars Orbiter Camera (MOC) observations of repeated Martian weather phenomena during the northern summer season. J. Geophys. Res. 107 (E3), 5014. https://doi.org/10.1029/2001JE001588.

Chapman, R.M., Lewis, S.R., Balme, M., Steels, L.J., 2017. Diurnal variation in Martian dust devil activity. Icarus 292, 154–167.

Clancy, R.T., Grossman, A.W., Wolff, M.J., James, P.B., Billawalla, Y.N., Sandor, B.J., Lee, S.W., Rudy, D.J., 1996. Water vapor saturation at low altitudes around Mars aphelion: a key to Mars climate? Icarus 122, 36–62.

Clancy, R.T., Wolff, M.J., Christensen, P.R., 2003. Mars aerosol studies with the MGS TES emission phase function observations: optical depths, particle sizes, and ice cloud types versus latitude and solar longitude. J. Geophys. Res. 108 (E9), 5097–5120.

Clancy, R.T., Wolff, M.J., Whitney, B.A., Cantor, B.A., Smith, M.D., McConnochie, T.H., 2010. Extension of atmospheric dust loading to high altitudes during the 2001 Mars dust storm: MGS TES limb observations. Icarus 207, 98–109.

Clancy, R.T., Montmessin, F., Benson, J., Daerden, F., Colaprete, A., Wolff, M.J., 2017. Mars clouds. In: Haberle, R.M., Clancy, R.T., Forget, F., Smith, M.D., Zurek, R.W. (Eds.), The Atmosphere and Climate of Mars. Cambridge University Press, Cambridge, UK, pp. 76–105.

Conrath, B., Curran, R., Hanel, R., Kunde, V., Maguire, W., Pearl, J., Pirraglia, J., Welker, J., 1973. Atmospheric and surface properties of Mars obtained by infrared spectroscopy on Mariner 9. J. Geophys. Res. 78, 4267–4278.

Conrath, B.J., Pearl, J.C., Smith, M.D., Maguire, W.C., Christensen, P.R., Dason, S., Kaelberer, M.S., 2000. Mars global surveyor thermal emission spectrometer (TES) observations: atmospheric temperatures during aerobraking and science phasing. J. Geophys. Res. 105 (E4), 9509–9519. https://doi.org/10.1029/1999JE001095.

Davis, S.P., Abrams, M.C., Brault, J.W., 2001. Fourier Transform Spectrometry. Academic Press.

Douté, S., Ceamanos, X., Appéré, T., 2013. Retrieving atmospheric dust opacity on Mars by imaging spectroscopy at large angles. Planet. Space Sci. 85, 38–52.

Douté, S., et al., 2014. Monitoring atmospheric dust spring activity at high southern latitudes on Mars using OMEGA. Planet. Space Sci. 96, 1–21.

Forget, F., Hourdin, F., Fournier, R., Hourdin, C., Talagrand, O., Collins, M., Lewis, S.R., Readand, P.L., Huot, J.-P., 1999. Improved general circulation models of the Martian atmosphere from the surface to above 80 km. J. Geophys. Res. 104 (E10), 24155–24176.

Formisano, V., et al., 2005. The Planetary Fourier Spectrometer (PFS) onboard the European Mars Express mission. Planet. Space Sci. 53 (10), 963–974.

Giuranna, M., et al., 2005a. Calibration of the Planetary Fourier Spectrometer short wavelength channel. Planet. Space Sci. 53 (10), 975–991.

Giuranna, M., et al., 2005b. Calibration of the Planetary Fourier Spectrometer long wavelength channel. Planet. Space Sci. 53 (10), 993–1007.

Giuranna, M., Grassi, D., Formisano, V., Montabone, L., Forget, F., Zasova, L., 2008. PFS/MEX observations of the condensing $CO_2$ south polar cap of Mars. Icarus 197, 386–402.

Grassi, D., Ignatiev, N.I., Zasova, L.V., Maturilli, A., Formisano, V., et al., 2005. Methods for the analysis of data from the Planetary Fourier Spectrometer on the Mars Express

mission. Planet. Space Sci. 53, 1017–1034.
Greeley, R., White, B.R., Pollack, J.B., Iversen, J.B., Leach, R.N., 1981. Dust storms on Mars: considerations and simulations. Spec. Pap. Geol. Soc. Am. 186, 101–121.
Guzewich, S.D., Talaat, E.R., Toigo, A.D., Waugh, D.W., McConnochie, T., 2013. High altitude dust layers on Mars: observations with the thermal emission spectrometer. J. Geophys. Res. Planets 118, 1177–1194. https://doi.org/10.1002/jgre.20076.
Guzewich, S.D., Wilson, R.J., McConnochie, T.H., Toigo, A.D., Banfield, D.J., Smith, M.D., 2014. Thermal tides during the 2001 Martian global-scale dust storm. J. Geophys. Res. Planets 119, 506–519. https://doi.org/10.1002/2013JE004502.
Hansen, G.B., 2003. Infrared optical constants of Martian dust derived from Martian spectra. In: Sixth International Conference on Mars, July 20–25 2003, Pasadena, California, (abstract no. 3194).
Hansen, 2005. Personal Communication.
Hansen, G.B., McCord, T.B., Galileo NIMS Team, 1997. Optical properties of water ice below 200 K. In: 28th Annual Lunar and Planetary Science Conference, March 17–21, 1997, Houston, TX, pp. 505.
Heavens, N.G., Richardson, M.I., Kleinböhl, A., Kass, D.M., McCleese, D.J., Abdou, W., Benson, J.L., Schofield, J.T., Shirley, J.H., Wolkenberg, P.M., 2011a. Vertical distribution of dust in the Martian atmosphere during northern spring and summer: high-altitude tropical dust maximum at northern summer solstice. J. Geophys. Res. 116, E01007. https://doi.org/10.1029/2010JE003692.
Heavens, N.G., Richardson, M.I., Kleinböhl, A., Kass, D.M., McCleese, D.J., Abdou, W., Benson, J.L., Schofield, J.T., Shirley, J.H., Wolkenberg, P.M., 2011b. The vertical distribution of dust in the Martian atmosphere during northern spring and summer: observations by the Mars Climate Sounder and analysis of zonal average vertical dust profiles. J. Geophys. Res. 116, E04003. https://doi.org/10.1029/2010JE003691.
Heavens, N.G., McCleese, D.J., Richardson, M.I., Kass, D.M., Kleinböhl, A., Schofield, J.T., 2011c. Structure and dynamics of the Martian lower and middle atmosphere as observed by the Mars Climate Sounder: 2. Implications of the thermal structure and aerosol distributions for the mean meridional circulation. J. Geophys. Res. 116, E01010. https://doi.org/10.1029/2010JE003713.
Heavens, N.G., Johnson, M.S., Abdou, W.A., Kass, D.M., Kleinböhl, A., McCleese, D.J., Shirley, J.H., Wilson, R.J., 2014. Seasonal and diurnal variability of detached dust layers in the tropical Martian atmosphere. J. Geophys. Res. Planets 119, 1748–1774. https://doi.org/10.1002/2014JE004619.
Hinson, D.P., Wilson, R.J., 2004. Temperature inversions, thermal tides, and water ice clouds in the Martian tropics. J. Geophys. Res. 109, E01002. https://doi.org/10.1029/2003JE002129.
Horne, D., Smith, M.D., 2009. Mars global surveyor thermal emission spectrometer (TES) observations of variations in atmospheric dust optical depth over cold surfaces. Icarus 200, 118–128. https://doi.org/10.1016/j.icarus.2008.11.007.
Houben, H., Haberle, R.M., Young, R.E., Zent, A.P., 1997. Modeling the Martian seasonal water cycle. J. Geophys. Res. 102, 9069–9083.
Ignatiev, N.I., Grassi, D., Zasova, L.V., 2005. Planetary Fourier spectrometer data analysis: fast radiative transfer models. Planet. Space Sci. 53, 1035–1042.
James, P.B., Martin, L.J., Henson, J.R., Birch, P.V., 1990. Seasonal recession of Mars' south polar cap in 1986. J. Geophys. Res. 95, 1337–1341. https://doi.org/10.1029/JB095iB02p01337.
James, P.B., Kieffer, H.H., Paige, D.A., 1992. The seasonal cycle of carbon dioxide on Mars. In: Kieffer, H.H., Jakosky, B.M., Snyder, C.W., Matthews, M.S. (Eds.), Mars. Univ. of Ariz. Press, Tucson, pp. 934–968.
James, P.B., Hollingsworth, J.L., Wolff, M.J., Lee, S.W., 1999. North polar dust storms in early spring on Mars. Icarus 138, 64–73.
James, P.B., Bonev, B.P., Wolff, M.J., 2005. Visible albedo of Mars' south polar cap: 2003 HST observations. Icarus 174, 596–599.
Kahre, M.A., Murphy, J.R., Haberle, R.M., 2006. Modeling the Martian dust cycle and surface dust reservoirs with the NASA Ames general circulation model. J. Geophys. Res. (Planets) 111, E06008.
Kahre, M.A., Hollingsworth, J., Haberle, R.M., Murphy, J.R., 2008. Investigations of the variability of dust particle sizes in the Martian atmosphere using the NASA Ames general circulation model. Icarus 195 (2), 576–597. https://doi.org/10.1016/j.icarus.2008.01.023.
Kass, D.M., Kleinböhl, A., McCleese, D.J., Schofield, J.T., Smith, M.D., 2016. Interannual similarity in the Martian atmosphere during the dust storm season. Geophys. Res. Lett. 43, 6111–6118. https://doi.org/10.1002/2016GL068978.
Kleinböhl, A., et al., 2009. Mars Climate Sounder limb profile retrieval of atmospheric temperature, pressure, dust, and water ice opacity. J. Geophys. Res. 114, E10006. https://doi.org/10.1029/2009JE003358.
Kleinböhl, A., Schofield, J.T., Abdou, W.A., Irwin, P.G.J., de Kok, R.J., 2011. A single-scattering approximation for infrared radiative transfer in limb geometry in the Martian atmosphere. J. Quant. Spectrosc. Rad. Transfer 112, 1568–1580.
Kleinböhl, A., Friedson, A.J., Schofield, J.T., 2017. Two-dimensional radiative transfer for the retrieval of limb emission measurements in the Martian atmosphere. JQSRT 187, 511–522.
Kuzmin, R.O., Zabalueva, E.V., Evdokimiva, N.A., Christensen, P.R., 2012. Mapping of the water ice content within the Martian surficial soil on the periphery of the retreating seasonal northern polar cap based on the TES and the OMEGA data. J. Geophys. Res. 117, E00J19. https://doi.org/10.1029/2012JE004071.
Levenberg, K., 1944. A method for the solution of certain non-linear problems in least squares. The Quarterly of Applied Mathematics 2, 164–168.
Määttänen, A., Fouchet, T., Forni, O., Forget, F., Savijärvi, H., Gondet, B., Melchiorri, R., Langevin, Y., Formisano, V., Giuranna, M., Bibring, J.P., 2009. A study of the properties of a local dust storm with Mars Express OMEGA and PFS data. Icarus 201, 504–516.
Madeleine, J.-B., et al., 2012. Aphelion water-ice cloud mapping and property retrieval using the OMEGA imaging spectrometer onboard Mars Express. J. Geophys. Res. 117, E00J07. https://doi.org/10.1029/2011JE003940.
Marquardt, D.W., 1963. An algorithm for least-squares estimation of nonlinear parameters. J. Soc. Ind. Appl. Math. 11 (2), 431–441.
Martin, T.Z., Kieffer, H.H., 1979. Thermal infrared properties of the Martian atmosphere. 2. The 15-mm band measurements. J. Geophys. Res. 84, 2843–2852.
Martin, L.J., James, P.B., Dollfus, A., Iwasaki, K., Beish, J.D., 1992. Telescopic observations: visual, photographic, polarimetric. In: Kieffer, H.H., Jakosky, B.M., Snyder, C.W., Matthews, M.S. (Eds.), Mars. Univ. of Ariz. Press, Tucson, pp. 34–70.
Mateshvili, N., Fussen, D., Vanhellemont, F., Bingen, C., Dekemper, E., Loodts, N., Tetard, C., 2009. Water ice clouds in the Martian atmosphere: two Martian years of SPICAM nadir UV measurements. Planet. Space Sci. 57, 1022–1031. https://doi.org/10.1016/j.pss.2008.10.007.
McCleese, D.J., et al., 2010. Structure and dynamics of the Martian lower and middle atmosphere as observed by the Mars Climate Sounder: seasonal variations in zonal mean temperature, dust, and water ice aerosols. J. Geophys. Res. 115, E12016. https://doi.org/10.1029/2010JE003677.
McCleese, D.J., Kleinbohl, A., Kass, D.M., Schofield, J.T., Wilson, R.J., Greybush, S., 2017. Comparisons of observations and simulations of the Mars polar atmosphere. In: VI Mars Modeling and Observations Workshop, Granada, Spain.
Medvedev, A.S., Kuroda, T., Hartogh, P., 2011. Influence of dust on the dynamics of the Martian atmosphere above the first scale height. Aeolian Res. 3 (2), 145–156. https://doi.org/10.1016/j.aeolia.2011.05.001.
Millour, E., Forget, F., Spiga, A., Navarro, T., Madeleine, J.-B., Montabone, L., Pottier, A., Lefèvre, F., Montmessin, F., Chaufray, J.Y., Lopez-Valverde, M.A., Gonzalez-Galindo, F., Lewis, S.R., Read, P.L., Huot, J.P., Desjean, M.C., MCD/GCM development Team, 2015. The Mars Climate Database (MCD Version 5.2), European Planetary Science Congress 2015, Held 27 September–2 October, 2015 in Nantes. (FranceAbstract 10:EPSC2015-438).
Montabone, L., Forget, F., Millour, E., Wilson, R.J., Lewis, S.R., Cantor, B.A., Kass, D., Kleinböhl, A., Lemmon, M.T., Smith, M.D., Wolff, M.J., 2015. Eight-year climatology of dust optical depth on Mars. Icarus 251, 65–95. https://doi.org/10.1016/j.icarus.2014.12.034.
Montmessin, F., et al., 2004. Origin and role of water ice clouds in the Martian water cycle as inferred from a general circulation model. J. Geophys. Res. 109, E10004. https://doi.org/10.1029/2004JE002284.
Montmessin, F., Quémerais, E., Bertaux, J.L., Korablev, O., Rannou, P., Lebonnois, S., 2006. Stellar occultations at UV wavelengths by the SPICAM instrument: retrieval and analysis of Martian haze profiles. J. Geophys. Res. 111. https://doi.org/10.1029/2005JE002662.
Mulholland, D.P., Spiga, A., Listowski, C., Read, P.L., 2015. An assessment of the impact of local processes on dust lifting in Martian climate models. Icarus 252, 212–227.
Navarro, T., Madeleine, J.-B., Forget, F., Spiga, A., Millour, E., Montmessin, F., Määttänen, A., 2014. Global climate modeling of the Martian water cycle with improved microphysics and radiatively active water ice clouds. J. Geophys. Res. Planets 119, 1479–1495 (doi: 10.10 02/2013JE0 04550).
Naylor, D.A., Tahic, M.K., 2007. Apodizing functions for Fourier transform spectroscopy. J. Opt. Soc. Am. A 24, 3644–3648.
Neary, L., Daerden, F., 2017. The GEM-Mars general circulation model for Mars: description and evaluation. Icarus 300, 458–476.
Neubauer, F.M., 1966. Thermal convection in the Martian atmosphere. J. Geophys. Res. 71, 2419–2426.
Neumann, G.A., Wilson, R.J., 2006. Night and day: the opacity of clouds measured by the Mars Orbiter Laser Altimeter (MOLA). Lunar Planet. Sci. XXXVII (abstract 2330).
Newman, C.E., Lewis, S.R., Read, P.L., Forget, F., 2002. Modeling the Martian dust cycle 2. Multiannual radiatively active dust transport simulations. J. Geophys. Res. (Planets) 107 (E12), 5124.
Pankine, A.A., Tamppari, L.K., Banfield, J.L., McConnochie, T.H., Smith, M.D., 2013. Retrievals of Martian atmospheric opacities from MGS TES nighttime data. Icarus 226, 708–722.
Pearl, J.C., Smith, M.D., Conrath, B.J., Bandfield, J.L., Christensen, P.R., 2001. Observations of Martian ice clouds by the Mars global surveyor thermal emission spectrometer: the first Martian year. J. Geophys. Res. 106 (E6), 12325–12338. https://doi.org/10.1029/1999JE001233.
Perrier, S., Bertaux, J.L., Lefèvre, F., Lebonnois, S., Korablev, O., Fedorova, A., Montmessin, F., 2006. Global distribution of total ozone on Mars from SPICAM/MEX UV measurements. J. Geophys. Res. 111, E09S06. https://doi.org/10.1029/2006JE002681.
Rannou, P., Perrier, S., Bertaux, J.-L., Montmessin, F., Korablev, O., Rébérac, A., 2006. Dust and cloud detection at the Mars limb with UV scattered sunlight with SPICAM. J. Geophys. Res. 111. https://doi.org/10.1029/2006JE002693.
Richardson, M.I., Wilson, R.J., 2002. A topographically forced asymmetry in the Martian circulation and climate. Nature 416, 298–301.
Richardson, M.I., Wilson, R.J., Rodin, A.V., 2002. Water ice clouds in the Martian atmosphere: general circulation model experiments with a simple cloud scheme. J. Geophys. Res. 107. https://doi.org/10.1029/2001JE001804.
Rodgers, C.D., 2000. Inverse Methods for Atmospheric Sounding: Theory and Practice. World Scientific, Singapore.
Rothman, L.S., et al., 2013. The HITRAN2012 molecular spectroscopic database. J. Quant. Spectrosc. Radiat. Transf. 130, 4–50.
Saggin, B., Scaccabarozzi, D., Tarabini, M., 2011. Instrumental phase-based method for Fourier transform spectrometer measurements processing. Appl. Opt. 50 (12), 1717–1725.
Siili, T., Haberle, R.M., Murphy, J.R., Savijarvi, H., 1999. Modelling of the combined late-winter ice cap edge and slope winds in Mars Hellas and Argyre regions. Planet. Space Sci 47 (8–9), 951–970.
Smith, M.D., 2004. Interannual variability in TES atmospheric observations of Mars

during 1999–2003. Icarus 167, 148–165.
Smith, M.D., 2008. Spacecraft observations of the Martian atmosphere. Annu. Rev. Earth Planet. Sci. 36, 191–219.
Smith, M.D., 2009. THEMIS observations of Mars aerosol optical depth from 2002–2008. Icarus 202, 444–452.
Smith, M.D., Pearl, J.C., Conrath, B.J., Christensen, P.R., 2000. Mars global surveyor thermal emission spectrometer (TES) observations of dust opacity during aerobraking and science phasing. J. Geophys. Res. 105, 9539–9552.
Smith, M.D., Bandfield, J.L., Christensen, P.R., Richardson, M.I., 2003. Thermal emission imaging system (THEMIS) infrared observations of atmospheric dust and water ice cloud optical depth. J. Geophys. Res. 108. https://doi.org/10.1029/2003JE002115.
Smith, M.D.M., Wolff, J., Clancy, R.T., Kleinböhl, A., Murchie, S.L., 2013. Vertical distribution of dust and water ice aerosols from CRISM limb-geometry observations. J. Geophys. Res. Planets 118, 321–334. https://doi.org/10.1002/jgre.20047.
Spiga, A., Lewis, S.R., 2010. Martian mesoscale and microscale wind variability of relevance for dust lifting. Int. J. Mars Sci. Explor. 5, 146–158.
Spiga, A., Faure, J., Madeleine, J.-B., Määttänen, A., Forget, F., 2013. Rocket dust storms and detached dust layers in the Martian atmosphere. J. Geophys. Res. Planets 118, 746–767. https://doi.org/10.1002/jgre.20046.
Stamnes, K., Tsay, S.C., Wiscombe, W., Jayaweera, K., 1988. Numerically stable algorithm for discrete-ordinate-method radiative transfer in multiple scattering and emitting layered media. Appl. Opt. 27 (12), 2502–2509.
Strausberg, M.J., Wang, H., Richardson, M.I., Ewald, S.P., Toigo, A.D., 2005. Observations of the initiation and evolution of the 2001 mars global dust storm. J. Geophys. Res. 110 (E2), E02006. https://doi.org/10.1029/20 04JE0 02361.
Tamppari, L.K., Zurek, R.W., Paige, D.A., 2003. Viking-era diurnal water-ice clouds. J. Geophys. Res. 108. https://doi.org/10.1029/2002JE001911.
Titus, T.N., 2005. Mars polar cap edges tracked over 3 full Mars years. Lunar Planet. Sci. XXXVI (Abstract 1993).
Titus, T.N., Cushing, G.E., 2014. Monitoring the Mars Polar Caps during Mars Years 24–28. (45th LPSC, abstract #2177).
Toigo, A.D., Richardson, M.I., 2000. Seasonal variation of aerosols in the Martian atmosphere. J. Geophys. Res. 105, 4109–4121.
Toigo, A.D., Richardson, M.I., Wilson, R.J., Wang, H., Ingersoll, A.P., 2002. A first look at dust lifting and dust storms near the south pole of Mars with a mesoscale model. J. Geophys. Res. 107 (E7), 5050. https://doi.org/10.1029/2001JE001592.
Wagstaff, K.L., Titus, T.N., Ivanov, A.B., Castaño, R., Bandfield, J.L., 2008. Observations of the north polar water ice annulus on Mars using THEMIS and TES. Planet. Space Sci. 56, 256–265.
Wang, H., Ingersoll, A.P., 2002. Martian clouds observed by Mars global surveyor Mars orbiter camera. J. Geophys. Res. 107 (E10), 5078. https://doi.org/10.1029/2001JE001815.
Wang, H.R., Richardson, M.I., Wilson, J.R., Ingersoll, A.P., Toigo, A.D., Zurek, R.W., 2003. Geophys. Res. Lett. 30 (9). https://doi.org/10.1029/2002GL016828. 1488.
Willame, Y., Vandaele, A.C., Depiesse, C., Lefèvre, F., Letocart, V., Gillotay, D., Montmessin, F., 2017. Retrieving cloud, dust and ozone abundances in the Martian atmosphere using SPICAM/UV nadir spectra. Planet. Space Sci. 142, 9–25.
Wilson, R.J., 1997. A general circulation model simulation of the Martian polar warming. Geophys. Res. Lett. 24, 123–126.
Wilson, R.J., 2011. Dust cycle modeling with the GFDL Mars general circulation model. In: IV Mars Modeling and Observations Workshop, Granada, Spain, Paris, France.
Wilson, A., Chicarro, A., 2004. Mars Express: the scientific payload. In: Wilson, A. (Ed.), Scientific Coordination: Agustin Chicarro. ESA SP-1240. ESA Publications Division, Noordwijk, Netherlands (XIV + 216 pp).
Wilson, R.J., Richardson, M.I., 2000. The Martian atmosphere during the Viking mission, I: infrared measurements of atmospheric temperature revisited. Icarus 145, 555–579.
Wilson, R.J., Neumann, G.A., Smith, M.D., 2007. Diurnal variation and radiative influence of Martian water ice clouds. Geophys. Res. Lett. 34, L02710. https://doi.org/10.1029/2006GL027976.
Wilson, R.J., et al., 2008. Influence of water ice clouds on Martian tropical atmospheric temperatures. Geophys. Res. Lett. 35 (7).
Wolff, M.J., Clancy, R.T., 2003. Constraints on the size of Martian aerosols from thermal emission spectrometer observations. J. Geophys. Res. 108 (E9), 5097–5120.
Wolff, R.T., et al., 2009. Wavelength dependence of dust aerosol single scattering albedo as observed by the compact reconnaissance imaging spectrometer. J. Geophys. Res. 114, E00D04. https://doi.org/10.1029/2009JE003350.
Wolkenberg, P., Smith, M.D., Formisano, V., Sindoni, G., 2011. Comparison of PFS and TES observations of temperature and water vapor in the Martian atmosphere. Icarus 215, 628–638.
Wolkenberg, P., Giuranna, M., Grassi, D., Aronica, A., Aoki, S., Scaccabarozzi, D., Saggin, B., 2018. Characterization of dust activity on Mars from MY27 to MY32 by PFS-MEX observations. Icarus 310, 32–47. https://doi.org/10.1051/0004-6361/201730903.
Zasova, L., Formisano, V., Moroz, V., Grassi, D., Ignatiev, N., et al., 2005. Water clouds and dust aerosols observations with PFS MEX at Mars. Planet. Space Sci. 53, 1065–1077.
Zurek, R.W., 1986. Atmospheric tidal forcing of the zonal-mean circulation: the Martian dusty atmosphere. J. Atmos. Sci. 43, 652–670.